

<sup>1</sup> DRAFT VERSION JUNE 21, 2018

[daniel.kocevski@nasa.gov](mailto:daniel.kocevski@nasa.gov)

[judith.racusin@nasa.gov](mailto:judith.racusin@nasa.gov)

2 Typeset using L<sup>A</sup>T<sub>E</sub>X preprint style in AASTeX62

3 Investigating the Nature of Late-Time High-Energy GRB Emission Through Joint  
4 *Fermi* /*Swift* Observations

5 M. AJELLO,<sup>1</sup> L. BALDINI,<sup>2</sup> G. BARBIELLINI,<sup>3,4</sup> D. BASTIERI,<sup>5,6</sup> R. BELLAZZINI,<sup>7</sup> E. BISSALDI,<sup>8,9</sup>  
6 R. D. BLANDFORD,<sup>10</sup> R. BONINO,<sup>11,12</sup> E. BOTTACINI,<sup>10</sup> J. BREGEON,<sup>13</sup> P. BRUEL,<sup>14</sup> R. BUEHLER,<sup>15</sup>  
7 R. A. CAMERON,<sup>10</sup> R. CAPUTO,<sup>16</sup> P. A. CARAVEO,<sup>17</sup> G. CHIARO,<sup>17</sup> S. CIPRINI,<sup>18,19</sup>  
8 J. COHEN-TANUGI,<sup>13</sup> D. COSTANTIN,<sup>6</sup> F. D'AMMANDO,<sup>20,21</sup> F. DE PALMA,<sup>9,22</sup> N. DI LALLA,<sup>2</sup>  
9 M. DI MAURO,<sup>10</sup> L. DI VENERE,<sup>8,9</sup> A. DOMÍNGUEZ,<sup>23</sup> C. FAVUZZI,<sup>8,9</sup> A. FRANCKOWIAK,<sup>15</sup>  
10 Y. FUKAZAWA,<sup>24</sup> S. FUNK,<sup>25</sup> P. FUSCO,<sup>8,9</sup> F. GARGANO,<sup>9</sup> D. GASPARRINI,<sup>18,19</sup> N. GIGLIETTO,<sup>8,9</sup>  
11 F. GIORDANO,<sup>8,9</sup> M. GIROLETTI,<sup>20</sup> D. GREEN,<sup>26,27</sup> I. A. GRENIER,<sup>28</sup> S. GUIRIEC,<sup>29,27</sup> C. HOLT,<sup>30</sup>  
12 D. HORAN,<sup>14</sup> G. JÓHANNESON,<sup>31,32</sup> D. KOCEVSKI,<sup>27</sup> M. KUSS,<sup>7</sup> G. LA MURA,<sup>6</sup> S. LARSSON,<sup>33,34</sup>  
13 J. LI,<sup>35</sup> F. LONGO,<sup>3,4</sup> F. LOPARCO,<sup>8,9</sup> P. LUBRANO,<sup>19</sup> J. D. MAGILL,<sup>26</sup> S. MALDERA,<sup>11</sup>  
14 A. MANFREDA,<sup>2</sup> M. N. MAZZIOTTA,<sup>9</sup> P. F. MICHELSON,<sup>10</sup> T. MIZUNO,<sup>36</sup> M. E. MONZANI,<sup>10</sup>  
15 A. MORSELLI,<sup>37</sup> M. NEGRO,<sup>11,12</sup> E. NUSS,<sup>13</sup> N. OMODEI,<sup>10</sup> M. ORIENTI,<sup>20</sup> E. ORLANDO,<sup>10</sup>  
16 V. S. PALIYA,<sup>1</sup> J. S. PERKINS,<sup>27</sup> M. PERSIC,<sup>3,38</sup> M. PESCE-ROLLINS,<sup>7</sup> F. PIRON,<sup>13</sup> G. PRINCIPE,<sup>25</sup>  
17 J. L. RACUSIN,<sup>27</sup> S. RAINÒ,<sup>8,9</sup> R. RANDO,<sup>5,6</sup> M. RAZZANO,<sup>7,39</sup> S. RAZZAQUE,<sup>40</sup> A. REIMER,<sup>41,10</sup>  
18 O. REIMER,<sup>41,10</sup> C. SGRÒ,<sup>7</sup> E. J. SISKIND,<sup>42</sup> G. SPANDRE,<sup>7</sup> P. SPINELLI,<sup>8,9</sup> D. TAK,<sup>26,27</sup>  
19 J. B. THAYER,<sup>10</sup> D. F. TORRES,<sup>35,43</sup> G. TOSTI,<sup>19,44</sup> J. VALVERDE,<sup>14</sup> M. VOGEL,<sup>45</sup> AND K. WOOD<sup>46</sup>

20 <sup>1</sup>*Department of Physics and Astronomy, Clemson University, Kinard Lab of Physics, Clemson, SC 29634-0978, USA*

21 <sup>2</sup>*Università di Pisa and Istituto Nazionale di Fisica Nucleare, Sezione di Pisa I-56127 Pisa, Italy*

22 <sup>3</sup>*Istituto Nazionale di Fisica Nucleare, Sezione di Trieste, I-34127 Trieste, Italy*

23 <sup>4</sup>*Dipartimento di Fisica, Università di Trieste, I-34127 Trieste, Italy*

24 <sup>5</sup>*Istituto Nazionale di Fisica Nucleare, Sezione di Padova, I-35131 Padova, Italy*

25 <sup>6</sup>*Dipartimento di Fisica e Astronomia “G. Galilei”, Università di Padova, I-35131 Padova, Italy*

26 <sup>7</sup>*Istituto Nazionale di Fisica Nucleare, Sezione di Pisa, I-56127 Pisa, Italy*

27 <sup>8</sup>*Dipartimento di Fisica “M. Merlin” dell’Università e del Politecnico di Bari, I-70126 Bari, Italy*

28 <sup>9</sup>*Istituto Nazionale di Fisica Nucleare, Sezione di Bari, I-70126 Bari, Italy*

29 <sup>10</sup>*W. W. Hansen Experimental Physics Laboratory, Kavli Institute for Particle Astrophysics and Cosmology,  
30 Department of Physics and SLAC National Accelerator Laboratory, Stanford University, Stanford, CA 94305, USA*

31 <sup>11</sup>*Istituto Nazionale di Fisica Nucleare, Sezione di Torino, I-10125 Torino, Italy*

32 <sup>12</sup>*Dipartimento di Fisica, Università degli Studi di Torino, I-10125 Torino, Italy*

33 <sup>13</sup>*Laboratoire Univers et Particules de Montpellier, Université Montpellier, CNRS/IN2P3, F-34095 Montpellier,  
34 France*

35 <sup>14</sup>*Laboratoire Leprince-Ringuet, École polytechnique, CNRS/IN2P3, F-91128 Palaiseau, France*

36 <sup>15</sup>*Deutsches Elektronen Synchrotron DESY, D-15738 Zeuthen, Germany*

37 <sup>16</sup>*Center for Research and Exploration in Space Science and Technology (CRESTT) and NASA Goddard Space Flight  
38 Center, Greenbelt, MD 20771, USA*

39 <sup>17</sup>*INAF-Istituto di Astrofisica Spaziale e Fisica Cosmica Milano, via E. Bassini 15, I-20133 Milano, Italy*

40 <sup>18</sup>*Space Science Data Center - Agenzia Spaziale Italiana, Via del Politecnico, snc, I-00133, Roma, Italy*

41 <sup>19</sup>*Istituto Nazionale di Fisica Nucleare, Sezione di Perugia, I-06123 Perugia, Italy*

42 <sup>20</sup>*INAF Istituto di Radioastronomia, I-40129 Bologna, Italy*

43 <sup>21</sup>*Dipartimento di Astronomia, Università di Bologna, I-40127 Bologna, Italy*

44 <sup>22</sup>*Università Telematica Pegaso, Piazza Trieste e Trento, 48, I-80132 Napoli, Italy*

45 <sup>23</sup>*Grupo de Altas Energías, Universidad Complutense de Madrid, E-28040 Madrid, Spain*

46 <sup>24</sup>*Department of Physical Sciences, Hiroshima University, Higashi-Hiroshima, Hiroshima 739-8526, Japan*

- 47 <sup>25</sup>*Friedrich-Alexander-Universität Erlangen-Nürnberg, Erlangen Centre for Astroparticle Physics, Erwin-Rommel-Str.*  
 48 *1, 91058 Erlangen, Germany*
- 49 <sup>26</sup>*Department of Astronomy, University of Maryland, College Park, MD 20742, USA*
- 50 <sup>27</sup>*NASA Goddard Space Flight Center, Greenbelt, MD 20771, USA*
- 51 <sup>28</sup>*Laboratoire AIM, CEA-IRFU/CNRS/Université Paris Diderot, Service d'Astrophysique, CEA Saclay, F-91191 Gif*  
 52 *sur Yvette, France*
- 53 <sup>29</sup>*The George Washington University, Department of Physics, 725 21st St, NW, Washington, DC 20052, USA*
- 54 <sup>30</sup>*Department of Physics and Center for Space Sciences and Technology, University of Maryland Baltimore County,*  
 55 *Baltimore, MD 21250, USA*
- 56 <sup>31</sup>*Science Institute, University of Iceland, IS-107 Reykjavik, Iceland*
- 57 <sup>32</sup>*Nordita, Roslagstullsbacken 23, 106 91 Stockholm, Sweden*
- 58 <sup>33</sup>*Department of Physics, KTH Royal Institute of Technology, AlbaNova, SE-106 91 Stockholm, Sweden*
- 59 <sup>34</sup>*The Oskar Klein Centre for Cosmoparticle Physics, AlbaNova, SE-106 91 Stockholm, Sweden*
- 60 <sup>35</sup>*Institute of Space Sciences (CSICIEEC), Campus UAB, Carrer de Magrans s/n, E-08193 Barcelona, Spain*
- 61 <sup>36</sup>*Hiroshima Astrophysical Science Center, Hiroshima University, Higashi-Hiroshima, Hiroshima 739-8526, Japan*
- 62 <sup>37</sup>*Istituto Nazionale di Fisica Nucleare, Sezione di Roma "Tor Vergata", I-00133 Roma, Italy*
- 63 <sup>38</sup>*Osservatorio Astronomico di Trieste, Istituto Nazionale di Astrofisica, I-34143 Trieste, Italy*
- 64 <sup>39</sup>*Funded by contract FIRB-2012-RBFR12PM1F from the Italian Ministry of Education, University and Research*  
 65 *(MIUR)*
- 66 <sup>40</sup>*Department of Physics, University of Johannesburg, PO Box 524, Auckland Park 2006, South Africa*
- 67 <sup>41</sup>*Institut für Astro- und Teilchenphysik and Institut für Theoretische Physik, Leopold-Franzens-Universität Innsbruck,*  
 68 *A-6020 Innsbruck, Austria*
- 69 <sup>42</sup>*NYCB Real-Time Computing Inc., Lattingtown, NY 11560-1025, USA*
- 70 <sup>43</sup>*Institució Catalana de Recerca i Estudis Avançats (ICREA), E-08010 Barcelona, Spain*
- 71 <sup>44</sup>*Dipartimento di Fisica, Università degli Studi di Perugia, I-06123 Perugia, Italy*
- 72 <sup>45</sup>*California State University, Los Angeles, Department of Physics and Astronomy, Los Angeles, CA 90032, USA*
- 73 <sup>46</sup>*Praxis Inc., Alexandria, VA 22303, resident at Naval Research Laboratory, Washington, DC 20375, USA*

## ABSTRACT

74

75 We use joint observations by the *Neil Gehrels Swift* X-ray Telescope (XRT) and the  
 76 *Fermi* Large Area Telescope (LAT) of gamma-ray burst (GRB) afterglows to investi-  
 77 gate the nature of the long-lived high-energy emission observed by *Fermi* LAT. Joint  
 78 broadband spectral modeling of XRT and LAT data reveal that LAT non-detections of  
 79 bright X-ray afterglows are consistent with a cooling break in the inferred electron syn-  
 80 chrotron spectrum below the LAT and/or XRT energy ranges. Such a break is sufficient  
 81 to suppress the high-energy emission so as to be below the LAT detection threshold.  
 82 By contrast, LAT-detected bursts are best fit by a synchrotron spectrum with a cooling  
 83 break that lies either between or above the XRT and LAT energy ranges. We spec-  
 84 ulate that the primary difference between GRBs with LAT afterglow detections and  
 85 the non-detected population may be in the type of circumstellar environment in which  
 86 these bursts occur, with late-time LAT detections preferentially selecting GRBs that  
 87 occur in low wind-like circumburst density profiles. Furthermore, we find no evidence of  
 88 high-energy emission in the LAT-detected population significantly in excess of the flux  
 89 expected from the electron synchrotron spectrum fit to the observed X-ray emission.  
 90 The lack of excess emission at high energies could be due to a shocked external medium  
 91 in which the energy density in the magnetic field is stronger than or comparable to that

of the relativistic electrons behind the shock, precluding the production of a dominant synchrotron self-Compton (SSC) component in the LAT energy range. Alternatively, the peak of the SSC emission could be beyond the 0.1–100 GeV energy range considered for this analysis.

*Keywords:* gamma-rays: bursts: general

## 1. INTRODUCTION

Joint observations by NASA’s *Neil Gehrels Swift* and *Fermi* missions have led to a unique opportunity to study the broadband properties of gamma-ray bursts (GRBs) over an unprecedentedly broad energy range. The two missions have the combined capability of probing the emission from GRBs over eleven decades in energy, ranging from optical ( $\sim 2$  eV) to high-energy gamma rays ( $> 300$  GeV). After more than 7 years of simultaneous operations, *Swift* and *Fermi* have detected thousands of GRBs, with over 100 of these bursts detected at energies greater than 30 MeV by the *Fermi* Large Area Telescope (LAT) (Vianello et al. 2015)<sup>1</sup>.

The properties of the high-energy emission observed by the LAT can differ considerably from the emission detected at keV and MeV energies by other instruments. While some bursts show evidence for emission in coincidence with activity at keV and MeV energies as observed by the *Swift* Burst Alert Telescope (BAT) and *Fermi* Gamma-ray Burst Monitor (GBM) (Ackermann et al. 2010), others also exhibit high-energy emission that is temporally extended, lasting longer than the emission observed at lower energies (Ackermann et al. 2013a, 2014). There also appears in some cases to be a delay in the onset of the LAT-detected emission with respect to the emission observed at lower energies (Abdo et al. 2009a,b; Ackermann et al. 2013b). The delayed onset and long-lived component of the LAT-detected emission suggest that GRB afterglows commonly observed in X-ray, optical, and radio wavelengths may also produce significant gamma-ray emission (Kumar & Barniol Duran 2009; Razzaque et al. 2010; Ghisellini et al. 2010; De Pasquale et al. 2010). In this interpretation, the coincident emission detected by the LAT is thought to be an extension of the prompt emission spectrum commonly attributed to shocks internal to the relativistic outflow (Ackermann et al. 2010; Maxham et al. 2011; Zhang et al. 2011; Yassine et al. 2017), while the late-time emission is due to the high-energy extension of the electron synchrotron spectrum produced by the external forward shock associated with the GRB blast wave moving into the circumstellar environment.

The properties of the high-energy emission observed by the LAT differ considerably from the emission detected at keV and MeV energies by other instruments. The high-energy emission is typically temporally extended, lasting longer than the emission observed at keV energies by both the *Swift* Burst Alert Telescope (BAT) and *Fermi* Gamma-Ray Burst Monitor (GBM). There also appears to be a consistent delay in the onset of the LAT-detected emission with respect to the emission observed at lower energies (Ackermann et al. 2013b). The delayed onset and long-lived nature of the LAT-detected emission suggest that the afterglow components commonly observed in X-ray, optical,

<sup>1</sup> [https://fermi.gsfc.nasa.gov/ssc/observations/types/grbs/lat\\_grbs/](https://fermi.gsfc.nasa.gov/ssc/observations/types/grbs/lat_grbs/)

131 and radio wavelengths may also produce significant gamma-ray emission (Kumar & Barniol Duran  
 132 2009; Razzaque et al. 2010; Ghisellini et al. 2010; De Pasquale et al. 2010). In this scenario, the late-  
 133 time emission detected by the LAT is due to the high-energy extension of the electron synchrotron  
 134 spectrum produced by the external forward shock associated with the GRB blast wave moving into  
 135 the circumstellar environment.

136 Broadband fits to the simultaneous multi-wavelength observations of GRB 110731A (Ackermann  
 137 et al. 2013a) and GRB 130427A (Ackermann et al. 2014) show similar late-time spectral and temporal  
 138 behavior, supporting such an external shock interpretation. Likewise, a stacking analysis of the LAT  
 139 data of *Swift*-localized bursts that were not detected above 40 MeV has shown evidence for sub-  
 140 threshold emission on timescales that far exceed the typical duration of the prompt emission at keV  
 141 energies (Beniamini et al. 2011; Ackermann et al. 2016). Furthermore, the strength of this high-  
 142 energy sub-threshold emission correlates directly with the X-ray brightness of the burst’s afterglow  
 143 emission, as measured by the *Swift* X-ray Telescope (XRT).

144 Despite the growing evidence for an external shock origin of the long-lived high-energy emission  
 145 observed by the LAT, the fact remains that only  $\sim 8\%$  of the bursts detected at keV energies within  
 146 the LAT field-of-view (FoV) have been detected above 40 MeV (Ackermann et al. 2013b). Therefore,  
 147 although the signature of the afterglow emission at X-ray wavelengths is largely ubiquitous in GRBs  
 148 observed by the XRT, the high-energy component is observed in only a small subset of these bursts.  
 149 This has led to speculation that LAT-detected bursts may represent a unique population of GRBs,  
 150 either probing a particular type of environment (Racusin et al. 2011; Beloborodov et al. 2014a), the  
 151 result of a unique set of afterglow conditions (Ghisellini et al. 2010), or the result of progenitors that  
 152 produce a rare class of hyper-energetic GRBs (Cenko et al. 2011).

153 In this paper we attempt to address the conditions that are required to produce the late time  
 154 high-energy emission detected by the LAT through the use of broadband data collected by both  
 155 *Swift* and *Fermi*. By examining joint XRT and LAT observations of 386 GRBs from 2008 August  
 156 4 to 2014 March 23, we can model the broadband spectra of the afterglow emission associated with  
 157 LAT-detected and non-detected GRBs. This allows us to determine if the relative sensitivities of the  
 158 XRT and LAT are sufficient to account for the majority of LAT non-detections, or whether the LAT-  
 159 detected bursts differ significantly in their afterglow properties from the general GRB population.  
 160 A subset of these bursts is also subjected to detailed broadband spectral fitting of the simultaneous  
 161 XRT and LAT data. From these spectral fits, we can determine whether the XRT and LAT data  
 162 are consistent with being drawn from the same power-law segment (PLS) of an electron synchrotron  
 163 spectrum, or if a break or suppression of the high-energy emission is required to explain the LAT non-  
 164 detection. This analysis also allows us to place constraints on the existence of spectral components at  
 165 high energies that are in excess of that predicted by the electron synchrotron model, such as external  
 166 inverse Compton (EIC) (Fan & Piran 2006; He et al. 2012; Beloborodov et al. 2014b) and synchrotron  
 167 self-Compton (SSC) (Dermer et al. 2000; Zhang & Mészáros 2001; Sari & Esin 2001; Wang et al.  
 168 2013) contributions.

169 The paper is structured as follows: in §2, we review the characteristics of the *Fermi* LAT and  
 170 *Swift* XRT instruments. In §3, we define the GRB samples considered in this work and outline the  
 171 analysis performed in §4. We present the results in §5, and discuss the implications of our results in  
 172 §6. Unless specified otherwise, all temporal and spectral indices are defined as  $F_\nu \propto E^{-\beta} t^{-\alpha}$ , where  
 173  $\beta = \Gamma - 1$ , and  $\Gamma$  is the photon index.

## 2. INSTRUMENT OVERVIEW

### 2.1. Swift *BAT* and Swift *XRT*

The *Neil Gehrels Swift* observatory consists of the *BAT* (Barthelmy et al. 2005), the *XRT* (Burrows et al. 2005a), and the UltraViolet Optical Telescope (UVOT) (Roming et al. 2005). The *BAT* is a wide-field, coded mask gamma-ray telescope, covering a FoV of 1.4 sr and an imaging energy range of 15–150 keV. The instrument’s coded-mask allows for positional accuracy of 1–4 arcminutes within seconds of the burst trigger. The *XRT* is a grazing-incidence focusing X-ray telescope covering an energy range from 0.3–10 keV and providing a typical localization accuracy of  $\sim 1$ –3 arcseconds.

*Swift* operates autonomously in response to *BAT* triggers on new GRBs, automatically slewing to point the *XRT* at a new source with 1–2 minutes. Data are promptly downloaded, and localizations are made available from the narrow-field instruments within minutes (if detected). *Swift* then continues to follow-up GRBs as they are viewable outside of observing constraints and the observatory is not in the South Atlantic Anomaly (SAA), for at least several hours after each burst, sometimes continuing for days, weeks, or even months if the burst is bright and of particular interest for follow-up.

### 2.2. Fermi *LAT*

The *Fermi Gamma-ray Space Telescope* consists of two scientific instruments, the *GBM* and the *LAT*. The *LAT* is a pair-conversion telescope comprising a  $4 \times 4$  array of silicon strip trackers and cesium iodide (CsI) calorimeters covered by a segmented anti-coincidence detector to reject charged-particle background events. The *LAT* detects gamma rays in the energy range from 20 MeV to more than 300 GeV with a FoV of  $\sim 2.4$  steradians, observing the entire sky every two orbits ( $\sim 3$  hours) while in normal survey mode. The deadtime per event of the *LAT* is nominally  $26 \mu\text{s}$ , the shortness of which is crucial for observations of high-intensity transient events such as GRBs. The *LAT* triggers on many more background events than celestial gamma-rays; therefore onboard background rejection is supplemented on the ground using event class selections that are designed to facilitate study of the broad range of sources of interest (Atwood et al. 2009).

In normal *Fermi* operations, the *GBM* triggers on new GRBs approximately every 1–2 days. The *LAT* survey mode rocking profile is occasionally interrupted (approximately once per month) by *GBM* initiating an autonomous repoint request (ARR) due to high-peak flux or fluence, which has proven to be an effective proxy for bright *LAT* bursts. The ARR causes *Fermi* to re-orient itself such that the *GBM* localization is placed at the center of the *LAT* FoV, where it remains for the next 2.5 hours, except when the GRB position is occulted the Earth. Roughly  $\sim 12$  GRBs per year simultaneously trigger both the *GBM* and *BAT*, but due to extended high-energy  $\gamma$ -ray emission observed by the *LAT* in some bursts, a GRB does not necessarily need to be in the *LAT* FoV at the trigger time to be detected. In normal survey mode, the *LAT* observes the position of every *GBM* and *BAT* detected burst within 3 hours.

## 3. SAMPLE DEFINITION

We compiled a sample of all GRBs observed by the *XRT* between the beginning of *Fermi* science operations on 2008 August 4 and 2014 March 23. The majority of bursts in the sample were observed by *LAT* during its normal survey observations at some time after the *BAT* trigger and the start of *XRT* observations. A small number of bursts were not observed by the *LAT* due to pointed

215 observations at the time of the GRB trigger. For each burst observed by the LAT, we selected good  
 216 time intervals (GTIs) during which the well-localized afterglow position was within  $65^\circ$  of the LAT  
 217 z-axis (boresight) beginning after the start of the first XRT observation and ending up to 20 ks post  
 218 trigger. The sensitivity of the LAT falls as a function of off-axis angle away from the instrument  
 219 boresight; therefore intervals during which the burst positions were  $> 65^\circ$  from the boresight were  
 220 not considered for this analysis. Neither XRT nor LAT take data during SAA passages; therefore we  
 221 also excluded intervals that occurred during these times. GRB positions that were at angles larger  
 222 than  $105^\circ$  with respect to the zenith direction for *Fermi*, placing the burst near the Earth’s limb,  
 223 were also excluded. Observations at such large zenith angles result in emission at the burst location  
 224 that are dominated by  $\gamma$ -rays from the Earth’s limb produced by interactions of cosmic rays with the  
 225 Earth’s atmosphere. The resulting sample includes a total of 1156 usable GTIs, for 386 GRBs.

## 226 4. ANALYSIS

### 227 4.1. XRT

228 For each burst, we obtained the XRT count-rate light curves from the public XRT team repository  
 229 hosted at the University of Leicester (Evans et al. 2007, 2009) and applied the de-absorbed counts-  
 230 to-energy-flux conversion factor as determined by the automated late-time spectral fits to the XRT  
 231 data. Since the XRT coverage and the LAT GTIs may not always overlap, we fit the XRT light curves  
 232 with a semi-automated light curve fitting routine (Racusin et al. 2009, 2011, 2016) with power laws  
 233 or broken power laws and gaussian flares (when flaring episodes are present), in order to estimate  
 234 the X-ray flux during XRT data gaps associated with periods of Earth occultation. We then use  
 235 the afterglow’s time-integrated photon index and associated error to convert the XRT energy flux  
 236 light curve in the 0.3–10 keV energy range to an extrapolated energy flux light curve in the 0.1–  
 237 100 GeV energy range. Note that by selecting only bursts for which there were LAT observations  
 238 after the start of XRT observations, we avoid the highly uncertain activity of both extrapolating  
 239 backward in time and to higher energies. Given the observations of both spectral and temporal  
 240 variability in early afterglow light curves, including energetic X-ray flares and plateaus followed by  
 241 sharp drops in flux, this decision avoids making any assumptions about the X-ray behavior prior to  
 242 the onset of the XRT observations even though it excludes several well-observed LAT bursts for which  
 243 subsequent XRT observations were made via *Swift* target of opportunity requests (e.g., GRB 080916C  
 244 and GRB 090926A).

### 245 4.2. LAT

246 For each interval in which the GRB was in the LAT FoV, we calculate the 95% confidence level  
 247 upper limits, or the observed energy flux with 68% errors, in the 0.1–100 GeV energy range for  
 248 LAT non-detections and detections respectively. We then compare these values to the expected  
 249 energy flux in the 0.1 to 100 GeV energy range from the fit to the XRT data. The LAT flux  
 250 estimates are obtained by performing an unbinned likelihood analysis using the standard analysis tools  
 251 (ScienceTools version v10r01p0)<sup>2</sup>. For this analysis, we used the ‘P8R2\_SOURCE\_V6’ instrument  
 252 response functions and selected ‘Source’ class events from a  $12^\circ$  radius energy-independent region  
 253 of interest (ROI) centered on the burst location. The size of the ROI is chosen to reflect the 95%  
 254 containment radius of the LAT energy-dependent point spread function (PSF) at 100 MeV. The

<sup>2</sup> <http://fermi.gsfc.nasa.gov/ssc/>

255 ‘Source’ event class was specifically optimized for the study of point-like sources, with stricter cuts  
 256 against non-photon background contamination relative to the ‘Transient’ event class that is typically  
 257 used to study GRBs on very short timescales (Ackermann et al. 2012a).

258 In standard unbinned likelihood fitting of individual sources, the observed distribution of counts  
 259 for each burst is modeled as a point source using an energy-dependent LAT PSF and a power-  
 260 law source spectrum with a normalization and photon index that are left as free parameters. For  
 261 the purposes of comparing the XRT extrapolation to the LAT data, we fixed the model’s photon  
 262 index to match the value measured by the XRT. In addition to the point source, Galactic and  
 263 isotropic background components are also included in the model, as well as all gamma-ray sources  
 264 in the 3FGL catalog within a source region with a radius of  $30^\circ$  centered on each ROI (Acero et al.  
 265 2015). The Galactic component, *gll\_iem\_v06*, is a spatial and spectral template that accounts for  
 266 interstellar diffuse gamma-ray emission from the Milky Way. The normalization of the Galactic  
 267 component is kept fixed during the fit. The isotropic component, *iso\_source\_v06*, provides a spectral  
 268 template to account for all remaining isotropic emission including contributions from both residual  
 269 charged particle backgrounds and the isotropic celestial gamma-ray emission. The normalization of  
 270 the isotropic component is allowed to vary during the fit. Both the Galactic and isotropic templates  
 271 are publicly available<sup>3</sup>.

272 We employ a likelihood-ratio test (Neyman & Pearson 1928) to quantify whether there exists a  
 273 significant excess of counts above the expected background. We form a test statistic (TS) that  
 274 is twice the ratio of the likelihood evaluated at the best-fit parameters under a background-only,  
 275 null hypothesis, i.e., a model that does not include a point source component, to the likelihood  
 276 evaluated at the best-fit model parameters when including a candidate point source at the center of  
 277 the ROI (Mattox et al. 1996). According to Wilks’ theorem (Wilks 1938), this ratio is distributed  
 278 approximately as  $\chi^2$ , so we choose to reject the null hypothesis when the test statistic is greater than  
 279  $TS = 16$ , roughly equivalent to a  $4\sigma$  rejection criterion for a single degree of freedom. Using this  
 280 test statistic as our detection criterion, we estimate the observed LAT flux for bursts with  $TS > 16$   
 281 and use a profile likelihood method described in more detail in Ackermann et al. (2012b) to calculate  
 282 upper limits for GRBs with  $TS < 15$ .

### 283 4.3. Joint XRT/LAT Spectral Fits

284 For bursts with time intervals during which the high-energy flux extrapolation of the XRT data is  
 285 equivalent to, or exceeds, the measured LAT flux or upper limit for that period, we also performed  
 286 joint spectral fits to the XRT and LAT data to investigate the underlying shape of the spectral energy  
 287 distribution (SED). To simplify the analysis, we only considered intervals with contemporaneous XRT  
 288 and LAT data. We refer to this subsample of GTIs as our “spectroscopic” sample.

289 For these fits, the *Swift* XRT data, including relevant calibration and response files, were retrieved  
 290 from the HEASARC archive<sup>4</sup> and processed with the standard *Swift* analysis software (v3.8) included  
 291 in NASA’s HEASOFT software (v6.11). We use *gtbin* to generate the count spectrum of the observed  
 292 LAT signal and *gtbkg* to extract the associated background by computing the predicted counts from  
 293 all the components of the best-fit likelihood model except the point source associated with the GRB.  
 294 The LAT instrument response for each interval was computed using *gtrspgen*.

<sup>3</sup> <http://fermi.gsfc.nasa.gov/ssc/data/access/lat/BackgroundModels.html>

<sup>4</sup> <http://heasarc.gsfc.nasa.gov/docs/swift/archive/>



295 The spectral fits were performed using the *XSPEC* version 12.7.0 (Arnaud 1996). Because the  
 296 number of counts in the LAT energy bins is often in the Poisson regime, we use the PG-statistic  
 297 from *XSPEC*, since the standard  $\chi^2$  statistic is not a reliable estimator of significance for low counts.  
 298 For bursts with no detectable emission, the count spectra associated with the modeled signal cannot  
 299 exceed the background spectra.. *XSPEC* takes this into account by constraining the best-fit model  
 300 from over-predicting the signal counts in the LAT energy range. The resulting flux upper limits from  
 301 these background-only intervals help constrain the hardness of the spectral model.

302 For each time interval, we fit two functional forms to the XRT and LAT data; a single power law  
 303 (PL) and a broken power law (BPL) model. Each form is multiplied by models for both fixed Galactic  
 304 (phabs) and free intrinsic host (zphabs for bursts with known redshift, phabs otherwise) photoelectric  
 305 absorption, and a free cross-calibration constant. Assuming that any break in the spectrum between  
 306 the XRT and LAT regimes at late times would be associated with the synchrotron cooling frequency,  
 307 i.e. the frequency at which an electron’s cooling time equals the dynamical time of the system, we  
 308 require the two power-law indices in the BPL model to differ by  $\Delta\Gamma = 0.5$  in accordance with the  
 309 theoretical expectation for electron synchrotron radiation from a forward shock (Granot & Sari 2002).

310 We perform a nested model comparison in order to determine if the additional degrees of freedom  
 311 in the BPL model are warranted over a simpler PL model. Assuming there are  $n_{\text{alt}}$  additional  
 312 free parameters under the alternative model, then the alternative model is statistically preferred  
 313 at a confidence level according to the difference in the PG-statistic, hereafter referred to as  $\Delta\text{Stat}$ ,  
 314 between the two fits, which is expected to follow a  $\chi^2$  distribution for  $n_{\text{alt}}$  degrees-of-freedom in the  
 315 large sample limit. Requiring that the two power-law indices in the BPL model differ by  $\Delta\Gamma = 0.5$   
 316 results in a single extra degree of freedom (i.e., the break energy) compared to the PL null hypothesis.  
 317 Therefore, according to the  $\chi^2$  cumulative distribution function, a value of  $\Delta\text{PG-Stat} > 9$  would  
 318 represent a  $> 3\sigma$  improvement in the fit. We adopt this criterion as the threshold for a statistical  
 319 preference for a break in the high-energy spectrum.

## 320 5. RESULTS

### 321 5.1. XRT Flux Extrapolations

322 **Examples of comparisons between the XRT fluxes extrapolated into the 0.1 to 100**  
 323 **GeV energy range and the LAT observations for GRB 090813 and GRB 100614A are**  
 324 **shown in Figure 1. The error bars on this XRT-extrapolated LAT-band flux (hereafter**  
 325 **referred to as the XRT-extrapolated flux) take into account the propagation of uncertainty of**  
 326 **both the X-ray flux and photon index into the LAT energy range. Both bursts shown in Figure 1**  
 327 **exhibit bright X-ray afterglows, relatively hard photon indices, and were well observed by the LAT**  
 328 **soon after the onset of the afterglow decay. Neither burst was detected by the LAT, and the estimated**  
 329 **upper limits for the energy flux in the 0.1–100 GeV energy range are above or are consistent with**  
 330 **the expected flux given the extrapolation of the XRT spectrum.**

331 The results of performing the same analysis on all 1156 GTIs in our sample are shown in Figure  
 332 2. The plot shows the measured LAT flux, or upper limit, versus the XRT-extrapolated flux for a  
 333 given interval when the burst location was within the LAT FoV. The gold stars represent the LAT  
 334 detections in our sample, which consist of 14 GTIs for 11 GRBs. We note that all but one of these

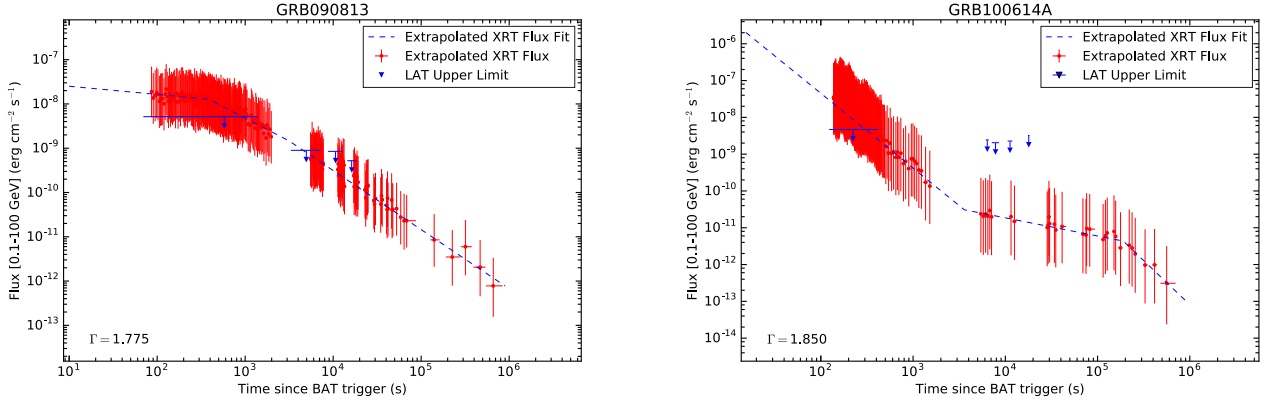


**Figure 1.** Examples of the comparison between the XRT-extrapolated flux and the LAT observations in the 0.1–100 GeV energy range for GRB 090813 and GRB 100614A. The  $\Gamma$  listed in the lower left corner indicates the time-averaged X-ray photon index used in the extrapolation. The blue dashed line represents the best-fit power-law segments to the X-ray afterglow flux. Neither burst was detected by the LAT despite both exhibiting bright X-ray afterglows, relatively hard photon indices, and being well observed by the LAT soon after the onset of the afterglow decay.

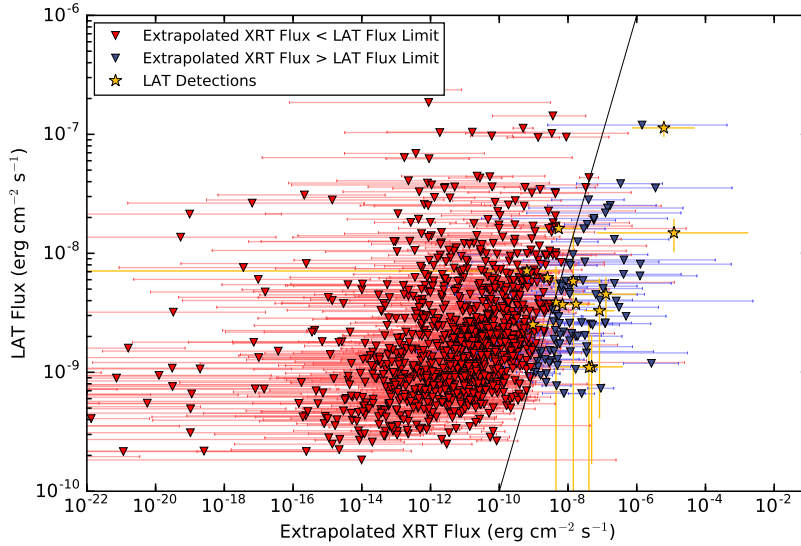


**Figure 2.** The measured LAT flux (yellow stars), or upper limit (downward triangles), versus the XRT-extrapolated flux for a given interval when the burst location was within the LAT FoV. The black line demarcates the equivalency. The blue and red colors of the downward triangles represent intervals when the extrapolated flux fell above and below the LAT flux measurements, respectively. The gold stars represent the LAT detections in our sample.

335 detections were announced via the Gamma-ray Coordinates Network (GCN)<sup>5</sup>, the two exceptions  
 336 being GRBs 081203A and 120729A, both of which were found through this analysis. Both these  
 337 bursts are discussed in greater detail in the 2nd *Fermi* LAT GRB catalog (The LAT Collaboration  
 338 2018, in prep)

<sup>5</sup> <https://gcn.gsfc.nasa.gov>

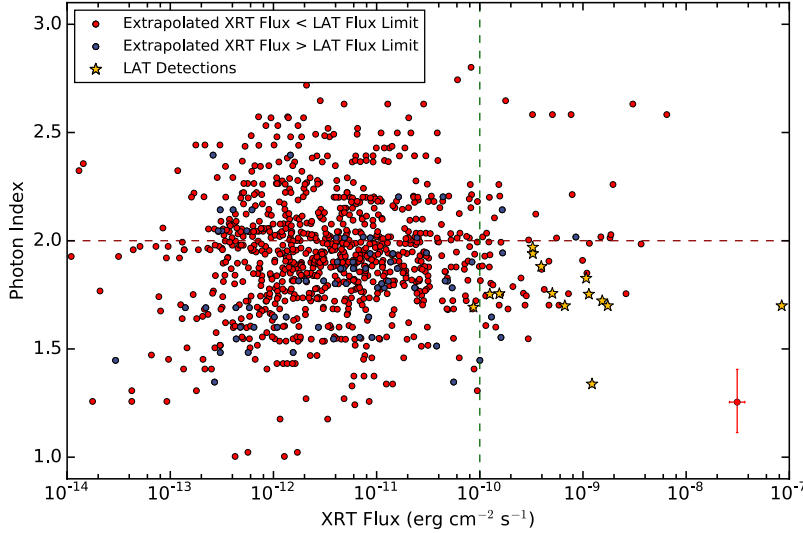


**Figure 3.** The time-average photon index  $\Gamma$  vs. the X-ray energy flux as measured by the XRT in the 0.3 to 10 keV energy range. The blue and red symbols represent intervals when the extrapolated flux fell above and below the LAT flux measurements, respectively, and the gold stars represent the LAT detections in our sample. The typical error bar is shown in the bottom right corner, and the vertical and horizontal dashed lines separate the plot into soft/hard and dim/bright quadrants.

339 For 91% of the intervals examined (1055 GTIs), the XRT-extrapolated flux in the LAT energy  
 340 range fell below the LAT upper limits (i.e. to the left of the equivalency line), and therefore were  
 341 consistent with the LAT non-detections. The extrapolated fluxes for an additional  $\sim 7\%$  (84 GTIs)  
 342 were above the LAT upper limits (i.e. to the right of the equivalency line). Interestingly, the flux  
 343 measurements for all of the LAT detections in our sample were either consistent with the XRT  
 344 extrapolation (4 GTIs) or fell below it (10 GTIs). None of the LAT detections showed evidence of  
 345 emission significantly in excess of the flux expected from the extrapolation of the XRT observations.

346 We examined the X-ray properties of the afterglows during these intervals in Figure 3, where we plot  
 347 the X-ray energy flux as measured by the XRT in the 0.3–10 keV energy range versus the associated  
 348 photon index  $\Gamma_{\text{XRT}}$ . The intervals with afterglow emission that would be expected to produce high-  
 349 energy emission in excess of the LAT sensitivity tend to be spectrally hard, with  $\Gamma_{\text{XRT}} \lesssim 2$ . They  
 350 are also drawn from a very wide range of fluxes. The LAT detections, on the other hand, are drawn  
 351 exclusively from afterglows that exhibited bright and hard emission, with criteria roughly fulfilling  
 352  $\Gamma_{\text{XRT}} \lesssim 2$  and  $F_{\text{XRT}} \gtrsim 10^{-10}$  erg cm $^{-2}$  s $^{-1}$  shown as dashed green lines. The red points that occupy  
 353 this quadrant of the plot did not have sufficiently deep upper limits for the expected high-energy flux  
 354 to exceed the LAT sensitivity, so their non-detections are consistent with the LAT observations. The  
 355 blue points, on the other hand, have deeper LAT upper limits, making their expected high-energy  
 356 emission inconsistent with the LAT observations.

357 We examine the properties of these afterglow intervals after folding in the LAT sensitivity in Figure  
 358 4, where we display the time-averaged photon indices for the afterglows, as measured by XRT, versus  
 359 the ratio of the XRT-extrapolated fluxes in the LAT energy range to the LAT upper limits (or  
 360 measured fluxes for detections). The colors of the symbols now represent the XRT energy fluxes  
 361 measured during the geometric mean of the afterglow interval. The geometric mean is defined as the  
 362 square root of the product of the interval start and end times. The green dashed line represents the

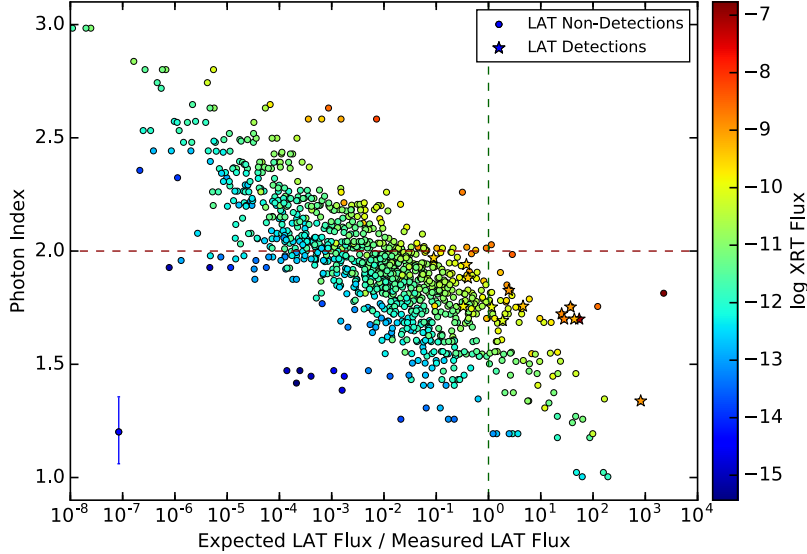


**Figure 4.** The time-averaged afterglow photon index, as measured by XRT, versus the ratio of the XRT-extrapolated flux in the LAT energy range to the LAT upper limit (or measured flux in the case of a detection). The colors of the symbols shows the XRT energy flux measured during the geometric mean of the afterglow interval, where the geometric mean is defined as the square root of the product of the interval start and end times. The green line represents the line of equivalency between the measured LAT flux (or upper limit) and the XRT-extrapolated flux. The typical error bar is shown in the bottom left corner, and the red dashed lines delineates the soft/hard populations and the green dashed line marks the line of equality between the expected and measured LAT flux.

363 line of equivalency between the measured LAT flux (or upper limit) and the XRT-extrapolated flux.  
 364 Bursts that fall to the right have X-ray extrapolations that are consistent with the LAT sensitivity,  
 365 whereas bursts that fall to the left have X-ray extrapolations that exceed the LAT flux measurements.  
 366 By construction, all of the blue data points in Figures 2 and 3 lie to the right of the green dashed  
 367 line. Again, a general trend is evident wherein the bursts with the hardest afterglow spectra and  
 368 highest observed XRT fluxes during the intervals in question are the bursts that result in X-ray  
 369 extrapolations that either exceed the LAT upper limits or result in LAT detections.

370 Figure 5 displays the same results, but now showing the ratio of the XRT-extrapolated flux to the  
 371 measured LAT flux (or upper limit) versus the geometric mean of the temporal interval in which  
 372 the burst position was within the LAT FoV. The colors of the symbols represents the time-averaged  
 373 photon index as measured by spectral fits to the late-time XRT data. The stars again represent the  
 374 LAT detections. Again, we see a general trend of bursts with harder afterglow spectra tending to  
 375 predict high-energy emission in excess of the LAT sensitivity. Although X-ray brightness correlates  
 376 strongly with the time of observation, Figure 5 demonstrates that many afterglows remain spectrally  
 377 hard to late times, resulting in afterglow emission that exceeds the LAT sensitivity thousands of  
 378 seconds after trigger. Likewise, the LAT detections appear in both early and late-time observations.

379 In order to understand what differentiates the afterglow intervals that have expected high-energy  
 380 emission that is inconsistent with the LAT observations from those with LAT detections, we selected  
 381 all intervals to the right of the line of equivalency in Figure 2 (i.e. the blue data points), as well as all  
 382 of the LAT-detected bursts (yellow data points), for which simultaneous XRT and LAT data exist.

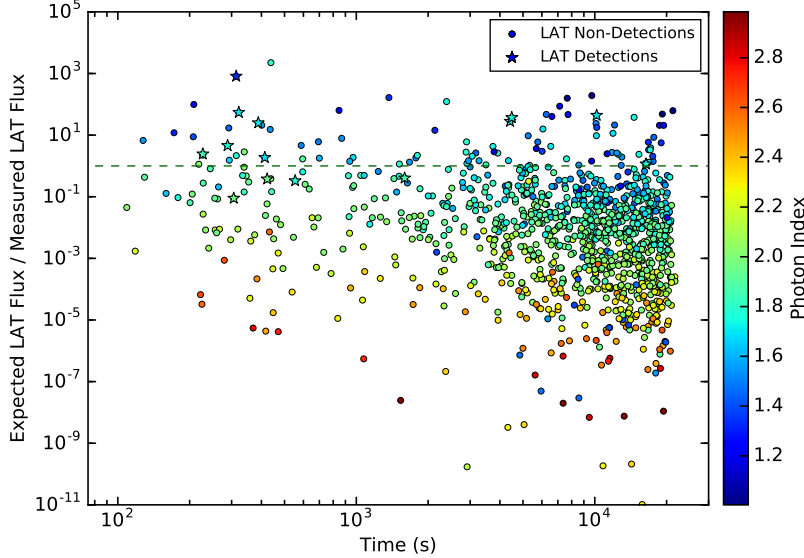


**Figure 5.** The ratio of the XRT-extrapolated flux to the measured LAT flux (or upper limit) vs. the geometric mean of the interval in which the burst position was within the LAT FoV. The colors of the symbols represents the time-average photon index as measured by spectral fits to the late-time XRT data and the stars represent the LAT detections. The vertical green dashed line represents the line of equality between the measured LAT flux (or upper limit) and the XRT-extrapolated flux.

383 A total of 64 GTIs for 52 bursts fulfill these criteria and form the spectroscopic sample for which we  
 384 performed additional joint spectral fits, described in the next section.

### 385 5.2. Joint XRT/LAT Spectroscopic Fits

386 Two examples of the joint spectroscopic fits performed using the contemporaneous XRT and LAT  
 387 data for GRB 130528A and GRB 100728A are shown in Figure 6. The measured XRT spectrum in  
 388 the 0.3 to 10 keV energy range is shown in red, while the LAT upper limits (95% confidence level)  
 389 are shown as blue downward arrows. The green and purple dashed lines represent fits to the data using  
 390 the single and broken power-law models described in §4.3. Neither GRB 130528A **nor** GRB 100728A  
 391 were detected by the LAT during the selected intervals (GRB 100728A was detected at an earlier  
 392 time), so upper limits are shown for emission in the 0.1 to 100 GeV energy range. Combined with the  
 393 XRT data, these limits constrain the broadband spectral shape of the afterglow emission from these  
 394 two bursts. In the case of GRB 130528A, a single power law covering eight orders of magnitude in  
 395 energy is consistent with both the XRT and LAT data, whereas a broken power-law is statistically  
 396 preferred in GRB 100728A, with an  $\sim 8\sigma$  ( $\Delta\text{PG-Stat} = 64.21$ ) improvement in the fit over a single  
 397 power law.

398 Of the 64 GTIs in our spectroscopic sample, a total of 52 intervals yielded no LAT-detected emission.  
 399 Of these 52 GTIs, 31 (60%) have simultaneous XRT and LAT data that are consistent with being  
 400 drawn from a spectral distribution that can be represented as a single power law. An additional  
 401 21 GTIs (40%) show a statistical preference, at greater than  $3\sigma$  significance, for a spectral break  
 402 between the XRT and LAT data. In all but one case, the LAT data can be accommodated by  
 403 either a power-law or a broken power-law, with a photon index change of  $\Delta\Gamma = 0.5$ , connecting the  
 404 contemporaneous XRT and LAT observations.

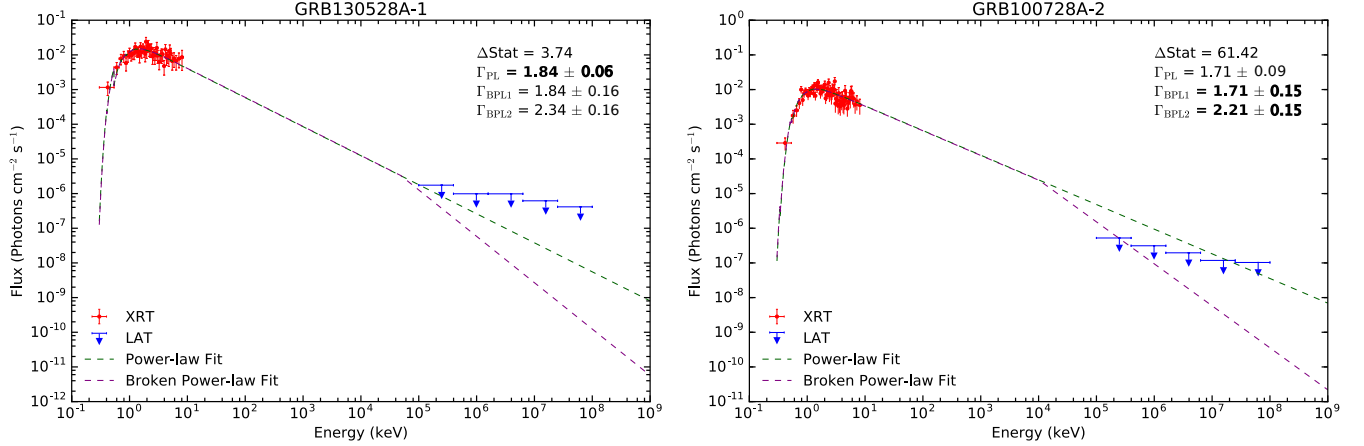


**Figure 6.** Joint spectroscopic fits performed using the contemporaneous XRT and LAT data for GRB 130528A and the second interval of GRB 100728A. The measured XRT spectrum in the 0.3 to 10 keV energy range is shown in red, while the LAT upper limits (95% confidence level) are shown as blue downward arrows. The green and purple dashed lines represent fits to the data using the single and broken power-law models. The photon indices from the preferred statistically preferred fit is shown in bold.

405 A median photon index of  $\Gamma_{\text{PL}} = 1.98 \pm 0.16$  was measured for the 31 GTIs for which a single  
 406 power law was adequate to describe both the XRT and LAT data, where we have adopt the standard  
 407 deviation of the sample as the error on the median. This is in contrast to the median photon index  
 408 of  $\Gamma_{\text{XRT}} = 1.68 \pm 0.21$  for this sample when measured from the XRT data alone. Therefore, adding  
 409 the LAT data to the spectral fit softens the estimated spectral shape for these bursts. For the bursts  
 410 which show a preference for a break in their broadband afterglow spectra, we find median XRT and  
 411 LAT photon indices of  $\Gamma_{\text{BPL1}} = 1.60 \pm 0.13$  and  $\Gamma_{\text{BPL2}} = 2.10$ , where the post break photon index is  
 412 fixed to  $\Gamma_{\text{BPL2}} = \Gamma_{\text{BPL1}} + 0.5$ . This is compared to the median photon index of  $\Gamma_{\text{XRT}} = 1.72 \pm 0.21$   
 413 for this sample when estimated from the XRT data alone. The median spectral fit results are summarized  
 414 in Table 1.

415

### 5.3. LAT Detections

416 The temporal and spectral fits for the 11 LAT-detected bursts with contemporaneous XRT and  
 417 LAT data in our spectroscopic sample are shown in the sub-panels of Figure 7. The spectral fits  
 418 were performed using data extracted from the first detected interval for each burst. Of the 11 bursts  
 419 analyzed, 5 show a preference for a break in their broadband spectrum between the XRT and LAT,  
 420 with the remainder 6 being consistent with a single power law from the X-ray to gamma-ray regimes.  
 421 As commented in §5.1, the flux measurements for all of the LAT detections were either consistent with  
 422 the XRT extrapolation or fell below it, which is confirmed by the joint spectral fits. The broadband  
 423 X-ray and gamma-ray spectral data for the LAT detections are all well fit by either a power-law or a  
 424 broken power-law model, and show no evidence of high-energy emission significantly in excess of the  
 425 flux expected from the XRT observations.

426 All of the LAT-detected bursts in our sample exhibit bright X-ray afterglows with relatively hard  
 427 X-ray photon indices (i.e.,  $\Gamma_{\text{XRT}} < 2$ ). A median photon index of  $\Gamma_{\text{PL}} = 1.77 \pm 0.04$  was measured  
 428 for the 6 GTIs for which a single power law was adequate to describe both the XRT and LAT data.  
 429 Unlike for the LAT non-detected bursts, this value is consistent with the median photon index of

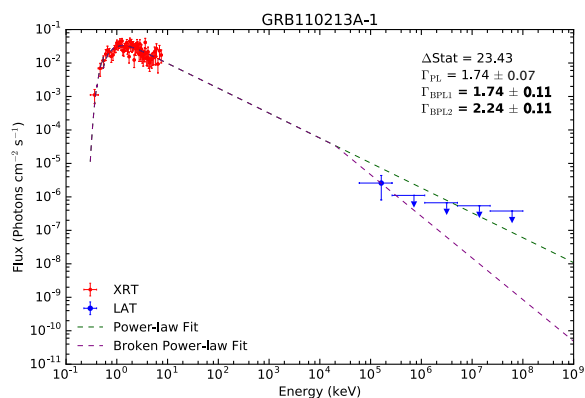
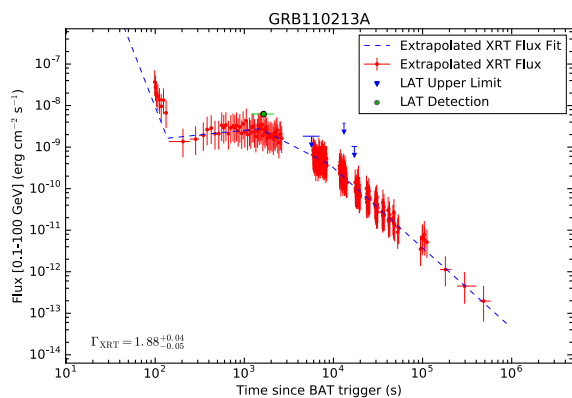
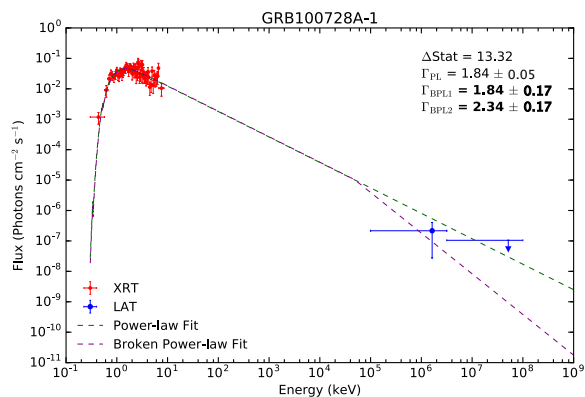
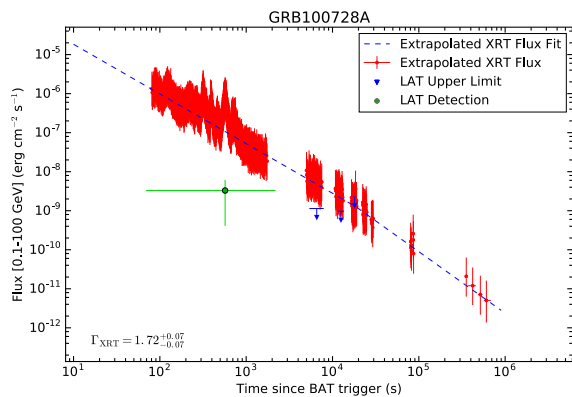
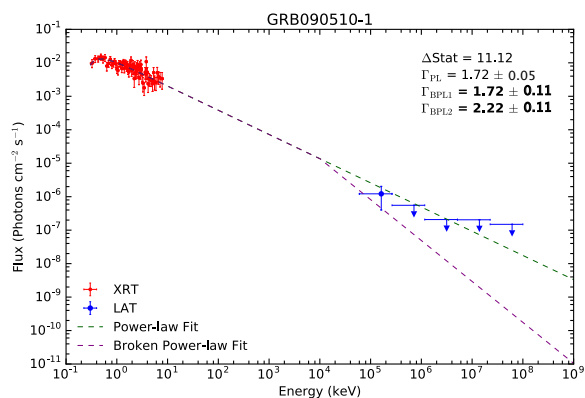
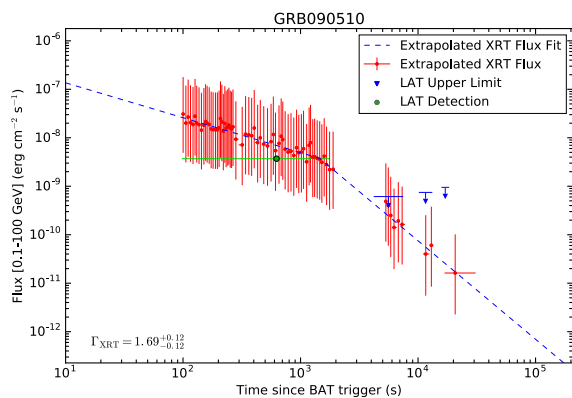
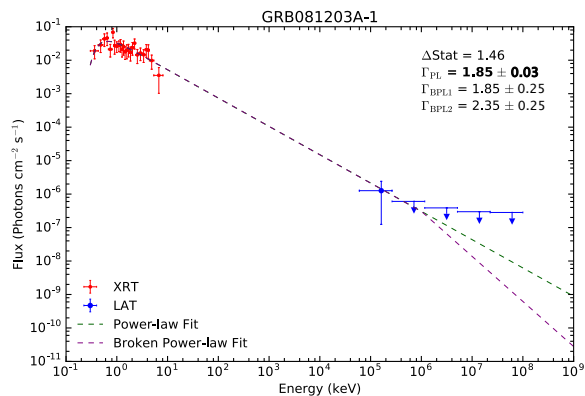
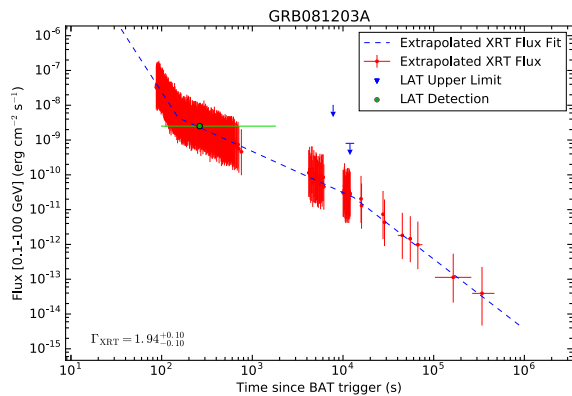
430  $\Gamma_{\text{XRT}} = 1.76 \pm 0.21$  for this sample when estimated from the XRT data alone. For the bursts which  
 431 show a preference for a break in their broadband afterglow spectrum, we find median XRT and  
 432 LAT photon indices of  $\Gamma_{\text{BPL1}} = 1.72 \pm 0.10$  and  $\Gamma_{\text{BPL2}} = 2.22$ . The pre-break photon index is again  
 433 consistent with the value estimated from the XRT data alone of  $\Gamma_{\text{XRT}} = 1.70 \pm 0.17$  for this sample.  
 434 The fit parameters for each individual LAT-detected burst are displayed in Table 2.

435 Our analysis reveals that a single power law is capable of explaining the broadband emission from  
 436 GRB 110731A, whereas the emission observed from GRB 130427A and GRB 090510 require a spectral  
 437 break between the X-ray and gamma-ray regimes. These results are consistent with those previously  
 438 reported by [Ackermann et al. \(2013a\)](#), [Kouveliotou et al. \(2013\)](#), and [De Pasquale et al. \(2010\)](#)  
 439 respectively. Conversely, we find that a spectral break is statistically preferred for GRB 100728A,  
 440 contrary to the findings of [Abdo et al. \(2011\)](#). In the latter case, the differing results can likely be  
 441 attributed to the greater sensitivity of the Pass 8<sup>6</sup> data selection used in this work, compared to the  
 442 Pass 7 data selection used in previous papers.

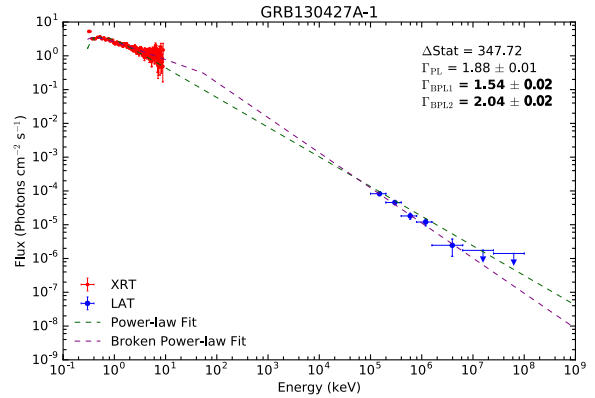
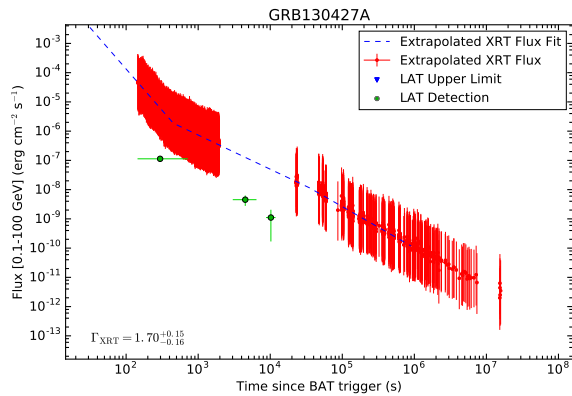
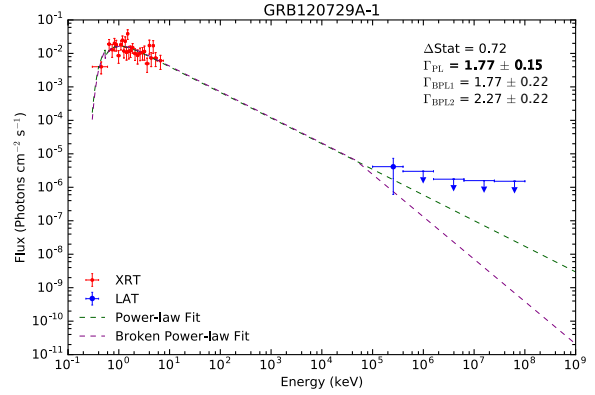
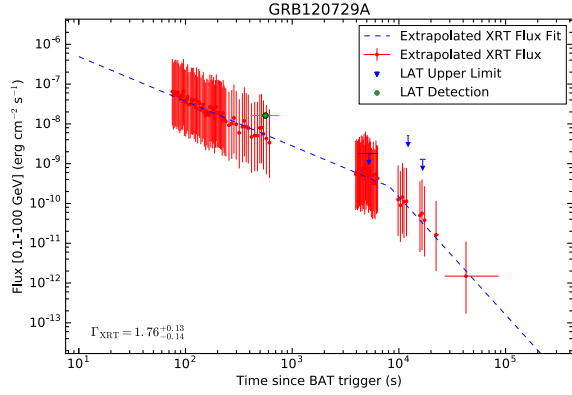
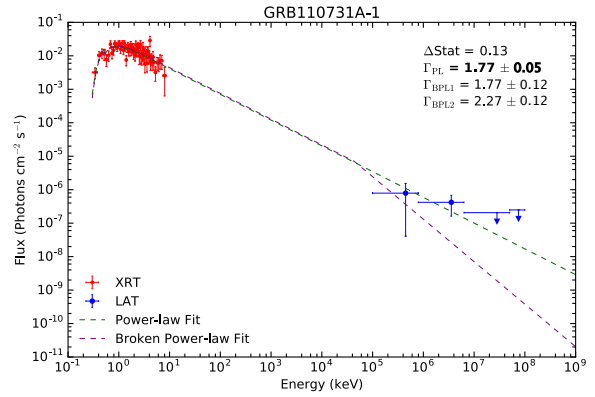
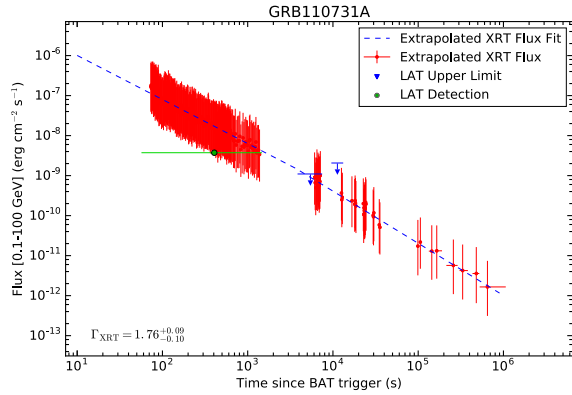
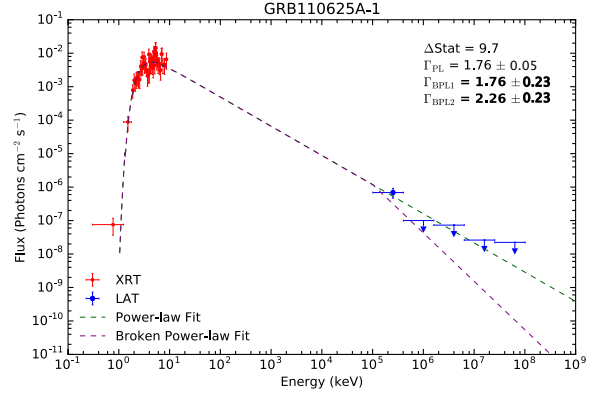
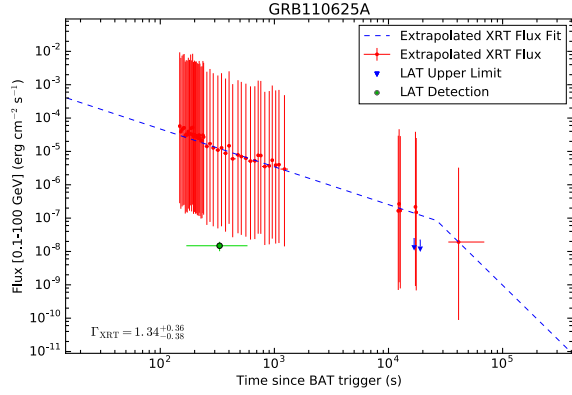
Sample	Best Fit	GTIs	$\Gamma_{\text{XRT}}$	$\Gamma_{\text{PL}}$	$\Gamma_{\text{BPL1}}$	$\Gamma_{\text{BPL2}}$
LAT Non-Detections	PL	31 (58%)	$1.68 \pm 0.21$	$1.98 \pm 0.16$	–	–
LAT Non-Detections	BPL	21 (40%)	$1.72 \pm 0.21$	–	$1.60 \pm 0.13$	2.10
LAT Detections	PL	6 (55%)	$1.76 \pm 0.21$	$1.77 \pm 0.04$	–	–
LAT Detections	BPL	5 (45%)	$1.70 \pm 0.17$	–	$1.72 \pm 0.10$	2.22

**Table 1.** A summary of the median best-fit parameters for the joint XRT/LAT spectral fits outlined in §5.2 and §5.3

<sup>6</sup> [https://fermi.gsfc.nasa.gov/ssc/data/analysis/documentation/Pass8\\_usage.html](https://fermi.gsfc.nasa.gov/ssc/data/analysis/documentation/Pass8_usage.html)







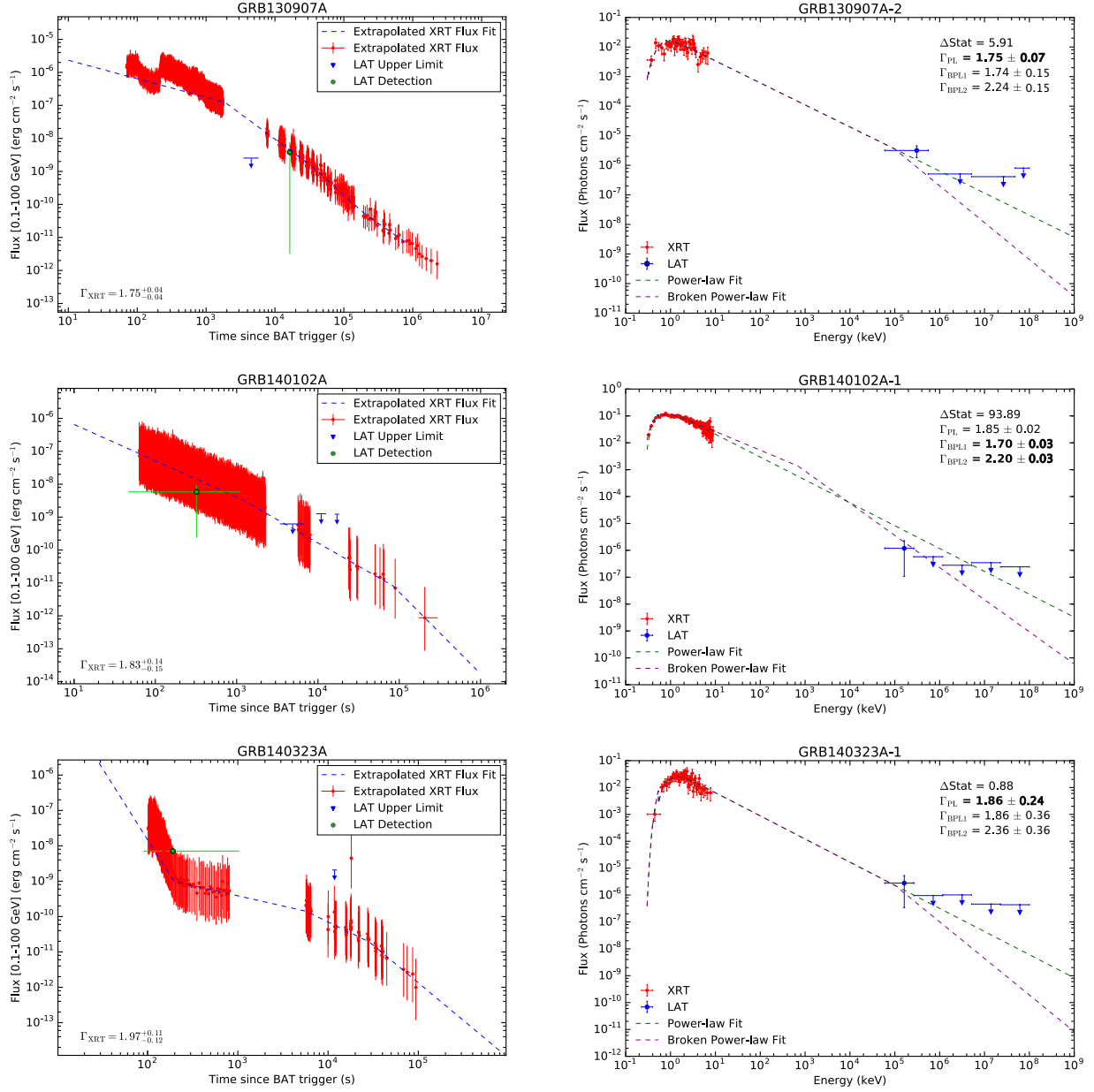


**Figure 7.** The temporal and spectral fits (left and right panels) for the 11 LAT-detected bursts with simultaneous XRT and LAT observations in our sample. The photon indices  $\Gamma_{\text{XRT}}$  listed on the temporal plots are derived from fits to only the time-integrated XRT data, whereas the photon indices listed on the spectral fits are obtained through the joint fits of both the XRT and LAT data. The numeric suffix in the title of the spectral plots indicates the temporal interval from which this data was extracted.

GRB	$\Gamma_{\text{XRT}}$	$\Gamma_{\text{LAT}}$	Best Fit	$\Delta\text{Stat}$	$\Gamma_{\text{PL}}$	$\Gamma_{\text{BPL1}}$	$\Gamma_{\text{BPL2}}$	$E_b$ (keV)
081203A	$1.94^{+0.10}_{-0.10}$	$2.18 \pm 0.36$	PL	1.5	$1.85 \pm 0.03$	$1.85 \pm 0.25$	2.35	–
090510A	$1.69^{+0.12}_{-0.12}$	$2.44 \pm 0.55$	BPL	11.1	$1.72 \pm 0.05$	$1.72 \pm 0.11$	2.22	$9958 \pm 968$
100728A	$1.72^{+0.07}_{-0.07}$	$1.70 \pm 0.22$	BPL	13.3	$1.84 \pm 0.05$	$1.84 \pm 0.17$	2.34	$9568 \pm 1045$
110213A	$1.88^{+0.04}_{-0.05}$	$1.60 \pm 0.36$	BPL	23.4	$1.74 \pm 0.07$	$1.74 \pm 0.11$	2.24	$10000 \pm 946$
110625A	$1.34^{+0.36}_{-0.38}$	$2.49 \pm 0.22$	BPL	9.7	$1.76 \pm 0.05$	$1.76 \pm 0.23$	2.26	$7125 \pm 1060$
110731A	$1.76^{+0.09}_{-0.10}$	$1.69 \pm 0.37$	PL	0.1	$1.77 \pm 0.05$	$1.77 \pm 0.12$	2.27	–
120729A	$1.76^{+0.13}_{-0.14}$	$1.77 \pm 0.35$	PL	0.7	$1.77 \pm 0.15$	$1.77 \pm 0.22$	2.27	–
130427A	$1.70^{+0.15}_{-0.16}$	$2.06 \pm 0.07$	BPL	347.7	$1.88 \pm 0.01$	$1.54 \pm 0.02$	2.04	$54 \pm 18$
130907A	$1.75^{+0.04}_{-0.04}$	$2.05 \pm 0.35$	PL	5.9	$1.75 \pm 0.07$	$1.74 \pm 0.15$	2.24	–
140102A	$1.83^{+0.14}_{-0.15}$	$1.53 \pm 0.31$	BPL	93.9	$1.85 \pm 0.02$	$1.70 \pm 0.03$	2.20	$681 \pm 16$
140323A	$1.97^{+0.11}_{-0.12}$	$1.86 \pm 0.42$	PL	0.9	$1.86 \pm 0.24$	$1.86 \pm 0.36$	2.36	–

**Table 2.** A summary of the best-fit spectral parameters for the LAT-detected population in our sample.  $\Gamma_{\text{XRT}}$  &  $\Gamma_{\text{LAT}}$  are the photon indices obtained from fitting the XRT and LAT GTIs separately, whereas  $\Gamma_{\text{PL}}$ ,  $\Gamma_{\text{BPL1}}$ , and  $\Gamma_{\text{BPL2}}$  are the photon indices obtained through the joint XRT and LAT fits to power-law (PL) and broken power-law (BPL) models, respectively. The post-break photon index in the BPL model is fixed to  $\Gamma_{\text{BPL2}} = \Gamma_{\text{BPL1}} + 0.5$ . A BPL model is statistically preferred at  $> 3\sigma$  over a simpler PL model when  $\Delta\text{Stat} > 9$ .

## 6. DISCUSSION

443

444 The results presented in §5.1 reveal that a majority of bursts that are detected by *Swift* XRT do  
 445 not have sufficiently bright afterglows and/or hard spectra to be detected by *Fermi* LAT. Of the  
 446 1156 intervals that we analyzed for this study, we found that only a small subset exhibited afterglow  
 447 emission that could exceed the LAT detection threshold when extrapolated to the 0.1 to 100 GeV  
 448 energy range. This finding illustrates that the late-time detection of afterglow emission by the LAT  
 449 at high energies is relatively uncommon, despite nearly every *Swift*-detected GRB being within the  
 450 LAT FoV at some point before the end of XRT observations. The bursts that do result in late-time  
 451 LAT detections exclusively have afterglow intervals with emission brighter than  $F_{\text{XRT}} \gtrsim 10^{-10}$  erg  
 452  $\text{cm}^{-2} \text{s}^{-1}$  and harder than  $\Gamma_{\text{XRT}} \lesssim 2$ .

453 We performed joint spectral fits of simultaneous XRT and LAT data for 52 GTIs for which no  
 454 emission was detected by the LAT, but for which their XRT derived afterglow spectra were sufficiently  
 455 bright and hard that they exceed the LAT upper limits. These fits reveal that a majority of these  
 456 cases (58%) can be explained by an afterglow spectrum with a slightly softer photon index when  
 457 constrained by both the XRT and LAT data, compared to the photon index derived by fits to the  
 458 XRT data alone. The remaining LAT non-detections required a break in their afterglow spectra  
 459 between the XRT and LAT energy ranges, consistent with a cooling break expected in the high-  
 460 energy regime of electron synchrotron emission from a relativistic blast wave expanding into an  
 461 external medium.

462 Of the 11 LAT-detected bursts in our sample, we find that the measured flux in the 0.1–100  
 463 GeV energy range is either consistent with, or falls below, the flux expected at these energies from  
 464 an extrapolation of their afterglow spectra as derived from simultaneous XRT observations. These  
 465 results are confirmed by joint spectral fits of XRT and LAT data for these bursts, which show that the

466 broadband X-ray and gamma-ray data are well fit by either a simple power-law, or a broken power-  
 467 law model that is consistent with a cooling break between the energy ranges of the two instruments.  
 468 As a result, we find no evidence of high-energy emission significantly in excess of the flux expected  
 469 from the spectrum predicted by the electron synchrotron model.

### 470 6.1. *On the Nature of the LAT-Detected Population*

471 An examination of the photon indices derived from the joint spectral fits for the LAT-detected and  
 472 non-detected bursts suggests a difference between these two populations. For the LAT non-detected  
 473 bursts, the median photon index of the spectral component connecting the XRT and LAT data is  
 474  $\Gamma_{\text{PL}} = 1.98 \pm 0.16$ . This value is consistent with the canonical value of  $\Gamma \sim 2$  expected from the high-  
 475 energy component of the electron synchrotron spectrum for both the slow and fast-cooling scenarios,  
 476 for an assumed power-law electron energy distribution of  $p = 2$ . Likewise, the LAT non-detected  
 477 bursts for which a break between the XRT and LAT was required have median pre- and post-break  
 478 power-law indices of  $\Gamma_{\text{BPL1}} = 1.6 \pm 0.13$  and  $\Gamma_{\text{BPL2}} = 2.1$ , again consistent with the expected  $\Gamma \sim 2$   
 479 post-break value. This indicates that the cooling break of the synchrotron spectrum lies either below  
 480 or between the XRT and LAT energy ranges for the LAT non-detections for which we performed  
 481 joint spectral fits.

482 By contrast, the LAT-detected bursts with broadband XRT and LAT data that are best fit by a  
 483 single power-law component yield a harder median photon index of  $\Gamma_{\text{PL}} = 1.77 \pm 0.04$ . The LAT-  
 484 detected bursts for which a break between the XRT and LAT was required have median values of  
 485 the pre- and post-break power-law indices  $\Gamma_{\text{BPL1}} = 1.72 \pm 0.10$  and  $\Gamma_{\text{BPL2}} = 2.22$ . The cooling break  
 486 of the synchrotron spectrum for these bursts appears to occur either between or above the XRT  
 487 and LAT energy ranges for a majority of the LAT-detected bursts. Not a single LAT-detected burst  
 488 examined in our analysis has an X-ray photon index that is consistent with the canonical  $\Gamma \sim 2$  value  
 489 expected for the highest-energy component predicted by an electron synchrotron spectrum in either  
 490 a slow or fast cooling regime.

491 The trend of LAT-detected bursts being spectrally harder in X-ray than their non-detected counter-  
 492 parts can be seen in an examination of the afterglow properties of all LAT-detected bursts observed  
 493 by the XRT. Figure 8 compares the photon index distributions of all LAT-detected GRBs for which  
 494 Swift XRT observations exist. A two-sided KS test yields a p-value of 0.0146, rejecting the hypothesis  
 495 that the two samples are drawn from the same distribution. Here we have dropped the requirement  
 496 that the LAT detection occurred after the start of the first XRT observations, because we are ex-  
 497 amining the properties of the afterglows of all LAT-detected bursts and are not making a joint  
 498 analysis between the two instruments. This allows us to include bursts such as GRBs 080916C and  
 499 090323A, which were detected by the LAT, but for which XRT observations began after the LAT  
 500 detections and were therefore excluded from our previous analysis. The X-ray photon index distri-  
 501 bution for all GRB afterglows observed by the XRT peaks at  $\Gamma_{\text{XRT}} \sim 2$ , indicating that the observed  
 502 emission is consistent with the highest-energy component predicted by an electron synchrotron spec-  
 503 trum in either the slow or fast cooling regimes. By contrast, the X-ray photon index distribution for  
 504 LAT-detected bursts peaks at a harder value of  $\Gamma_{\text{XRT}} \sim 1.8$ , again suggesting that the synchrotron  
 505 spectrum’s cooling break lies either between or above the XRT and LAT energy ranges for a majority  
 506 of the LAT-detected bursts.

507 A potentially important effect that we note is that the cooling break frequency ( $\nu_c$ ) in the afterglow  
 508 synchrotron spectrum is expected to be very smooth and possibly extend over  $\sim 2$ – $3$  decades in photon

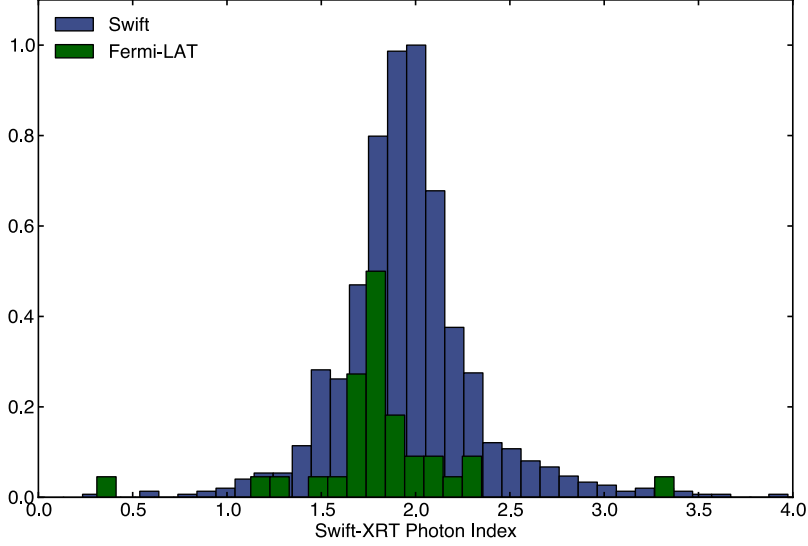


**Figure 8.** A comparison of the X-ray photon index distribution for all *Swift* XRT-detected GRBs (blue) and those detected by the LAT (green), for which *Swift* XRT observations exist.

509 energy (Granot & Sari 2002). Therefore, in some cases  $\nu_c$  might be either (i) near the XRT energy  
 510 range, in which case  $\Gamma_{\text{XRT}} > \Gamma_1$  will be inferred, with the spectral index measured by the LAT being  
 511  $\Gamma_{\text{LAT}} < \Gamma_2$ , resulting in a measured (or effective) spectral break  $\Delta\Gamma_{\text{eff}}$  that is less than the theoretical  
 512 prediction,  $\Delta\Gamma_{\text{eff}} = \Gamma_{\text{LAT}} - \Gamma_{\text{XRT}} < \Gamma_2 - \Gamma_1 = \Delta\Gamma$ , where  $\Gamma_2$  and  $\Gamma_1$  are the asymptotic values of the  
 513 photon index above and below the cooling break, respectively, or (ii)  $\nu_c$  can be near or within the LAT  
 514 energy range, in which case  $\Gamma_{\text{LAT}} < \Gamma_2$  can be inferred (while  $\Gamma_{\text{XRT}} = \Gamma_1$ ) so that again  $\Delta\Gamma_{\text{eff}} < \Delta\Gamma$ .  
 515 Therefore, imposing  $\Delta\Gamma = 0.5$  with a broken power-law spectrum may result in inferred  $\Gamma_2$  and  $\Gamma_1$   
 516 values that differ from their true values, and thus complicate direct comparison to the theoretical  
 517 prediction for the asymptotic value of  $\Gamma_2$ , which for  $p \sim 2-2.5$ , corresponds to  $\Gamma_2 \sim 2 - 2.25$ .

518 We examined the influence that a broad cooling break could have on our results by implementing  
 519 the smoothly broken power-law (SBPL) spectrum described in (Granot & Sari 2002), with a fixed  
 520 sharpness of the break set to  $s = 0.85$ . We fit this model to the XRT and LAT data for GRB 130427A  
 521 and obtained consistent pre and post break photon indices of  $\Gamma_{\text{BPL1}} = 1.54 \pm 0.02$  and  $\Gamma_{\text{BPL2}} =$   
 522  $2.04 \pm 0.02$ , whereas the SBPL model returned  $\Gamma_{\text{BPL1}} = 1.56 \pm 0.07$  and  $\Gamma_{\text{BPL2}} = 2.06 \pm 0.07$ . We  
 523 conclude that the large gap in energy between the XRT and LAT data effectively mask the effects  
 524 of the curvature in the break energy for the SBPL model as long as the spectral break is well within  
 525 the MeV domain, resulting in asymptotic photon indices in the XRT and LAT energy ranges which  
 526 are consistent with those obtained using the simpler BPL model. We present the break energies for  
 527 the six LAT detected bursts for which a BPL model was preferred over a PL model in Table 2 and  
 528 show that the break energies are well above the XRT domain or below the LAT domain, with the  
 529 exception of GRB 130427A, for which we explicitly fit the SBPL model and showed consistency with  
 530 the simpler BPL model.

## 531 6.2. Constraining the Circumstellar Environment of LAT-detected GRBs

532 The value and time evolution of the cooling frequency, i.e. the gyration frequency of an electron  
 533 whose cooling time equals the dynamical time of the system, in an electron synchrotron spectrum in  
 534 the slow-cooling regime is heavily dependent on the density profile  $\rho_{\text{ext}}(r) = A_* r^{-k}$  of the circumstellar

535 medium (Chevalier & Li 2000; Granot & Sari 2002). The cooling frequency is expected to evolve to  
 536 lower energies with time in a constant density interstellar medium (ISM) ( $k = 0$ ) profile, and evolve  
 537 to higher energies in a stellar wind ( $k = 2$ ) environment.

538 We speculate that the primary difference between the LAT-detected and non-detected populations  
 539 may be in the type of circumstellar environment in which these bursts occur. LAT detections may  
 540 be preferentially selecting GRBs that occur in low wind-like circumburst density profiles for which  
 541 the synchrotron cooling break begins near the X-ray regime and does not evolve to lower energies;  
 542 hence the afterglow spectrum above the X-ray regime that remains spectrally hard for longer periods  
 543 of time.

544 The inference that LAT-detected bursts may be preferentially occurring in wind-like environments  
 545 is consistent with an analysis of the multi-wavelength observations of both GRB 110731A (Ackermann  
 546 et al. 2013a) and GRB 130427A (Kouveliotou et al. 2013). Using data collected by the XRT, LAT and  
 547 the Nuclear Spectroscopic Telescope Array (*NuSTAR*), Kouveliotou et al. (2013) found that a break  
 548 between the X-ray and gamma-ray regimes best fits the broadband data for GRB 130427A at very  
 549 late times. The authors speculate that the cooling break in the afterglow spectra of GRB 130427A  
 550 may not have evolved with time and remained between the XRT and LAT energy ranges due to a  
 551 circumstellar density profile that is intermediate between ISM and wind-like circumstellar density  
 552 profiles.

553 Likewise, Ackermann et al. (2013a) performed broadband modeling of optical, UVOT, BAT, XRT,  
 554 and LAT data associated with GRB 110731A and found that initially a single power law adequately  
 555 fit the broadband SED using BAT, GBM and LAT data. **At a later time a spectral break was**  
 556 **observed between the XRT and LAT data**, which was interpreted as a cooling break evolving  
 557 from low to high frequencies for a GRB blast wave evolving in a wind-like environment. Although  
 558 they concluded that an observed break between the optical and X-ray data can be best explained  
 559 by the presence of a cooling break between the two regimes, the photon index of  $\Gamma = 1.77$  obtained  
 560 through our joint spectral fits for this burst suggests that this break lies above the LAT energy range.  
 561 Again, the differences between the Ackermann et al. (2013a) work and this analysis can be likely  
 562 attributed to the greater sensitivity at low energies of the Pass 8 data used in this work, although  
 563 we point out that our analysis does not include fits to optical data as were performed by Ackermann  
 564 et al. (2013a).

565 A preference for LAT-detected GRBs to occur in low density wind-like circumstellar environments  
 566 was also found by Cenko et al. (2011), who modeled the broadband spectral and temporal X-  
 567 ray, optical, and radio afterglow data of four LAT-detected GRBs: GRB 090323, GRB 090328,  
 568 GRB 090902B, and GRB 090926A. The authors found that a wind environment best fit the data for  
 569 all but GRB 090902B, for which a constant-density ISM environment was preferred. In this interpre-  
 570 tation, the relatively small number of *Swift* XRT-detected bursts that have the expected afterglow  
 571 behavior in a wind-like density profile (Schulze et al. 2011) may further explain the relatively small  
 572 number of LAT detections of bright XRT-detected afterglows.

### 573 6.3. Constraints on Inverse Compton Emission

574 The results summarized in Figure 2 significantly constrain the strength and ubiquity of inverse  
 575 Compton (IC) emission in the 0.1 to 100 GeV energy range during the XRT and LAT observations  
 576 that we considered. Such emission is a natural consequence of non-thermal relativistic blast waves  
 577 thought to power GRB afterglows, although a definitive detection of IC emission at GeV energies

578 has been elusive in the *Fermi* era. IC components can result from upscattering of soft X-ray photons  
 579 external to the relativistic blast wave, external inverse Compton (EIC) (Fan & Piran 2006; He et al.  
 580 2012; Beloborodov et al. 2014b), or synchrotron self-Compton (SSC) in which synchrotron-emitting  
 581 electrons in the relativistic blast wave upscatter their own synchrotron radiation (Dermer et al. 2000;  
 582 Zhang & Mészáros 2001; Sari & Esin 2001; Wang et al. 2013). The lack of significant emission in the  
 583 LAT energy range in excess of the flux expected from the spectra extrapolated from XRT observations  
 584 requires that any accompanying IC components must be subdominant to the high-energy tail of the  
 585 synchrotron spectrum, or peak above the LAT energy range we considered for this analysis.

586 We can examine these constraints more closely if we consider that the ratio of the peak flux of the  
 587 synchrotron and SSC components, or Compton  $Y$  parameter, in the slow-cooling regime, scales as  
 588  $\propto (\epsilon_e/\epsilon_B)^{1/2}(\gamma_m/\gamma_c)^{p-2}$ . Here  $\epsilon_e$  and  $\epsilon_B$  are the fractional-energy densities of the relativistic electrons  
 589 and magnetic field, and  $\gamma_m$  and  $\gamma_c$  represent the minimum injection energy and the typical electron  
 590 Lorentz factor above which the relativistic electrons radiate a significant fraction of their energy on  
 591 the dynamical timescale, respectively (Sari & Esin 2001). **A relativistic blast wave with a large**  
 592 **fraction of its total energy stored in energetic electrons (large  $\epsilon_e$ ) and/or low magnetic**  
 593 **field density (extremely small  $\epsilon_B$ ), is expected to generate prominent SSC emission,**  
 594 **which is in disagreement with our observations. This could point to a blast wave in the**  
 595 **synchrotron-dominated regime in which a larger fraction of its total energy is stored**  
 596 **in the magnetic field density (large  $\epsilon_B$ ) (Zhang & Mészáros 2001). Alternatively, the**  
 597 **blast wave could be in the Klein-Nishina dominated regime in which  $Y < 1$ , even though**  
 598  **$\epsilon_e/\epsilon_B \gg 1$  because of the Klein-Nishina reduction to the electron-photon scattering cross-**  
 599 **section. Both scenarios could suppress the SSC component, making it undetectable in**  
 600 **the LAT energy range.**

601 On the other hand, the peak frequency of the SSC component scales roughly as  $E_{pk}^{SSC} = \gamma_c^2 E_{pk}^{syn}$ ,  
 602 with  $E_{pk}^{syn} = E_c$  in the slow-cooling regime, where  $E_c$  is the energy of the cooling break. Therefore,  
 603 a non-detection of strong SSC emission could also imply that  $E_{pk}^{SSC}$  is beyond the LAT energy range  
 604 we considered. Assuming that  $E_{pk}^{syn}$  lies between or above the XRT and LAT energy range during  
 605 our observations, this could be accommodated with a moderate value of  $\gamma_c$  of 100–1000. **We note,**  
 606 **though, that since the SSC component is expected to span several orders of magnitude**  
 607 **in energy around  $E_{pk}^{SSC}$  (Sari & Esin 2001), requiring the spectral upturn due to the SSC**  
 608 **component to be above the LAT energy range is far more demanding. Likewise, the non-**  
 609 **detection of the SSC component at late times, when the cooling break has potentially**  
 610 **evolved into the X-ray regime, places even further constraints on this scenario.**

611 The widely discussed detection of high-energy photons with energies  $> 10$  GeV hours after the  
 612 onset of GRB 130427A has been attributed to SSC emission by Tam et al. (2013) and Wang et al.  
 613 (2013). Ackermann et al. (2014) and Kouveliotou et al. (2013), on the other hand, both argue that  
 614 the high-energy light curve and spectra are consistent with a single electron synchrotron spectrum  
 615 throughout the evolution of the extended emission. Here we draw similar conclusions from the three  
 616 intervals for which we compared the XRT and LAT data for GRB 130427A. The extension of the XRT  
 617 spectra over-predicts the emission expected in the 0.1 to 100 GeV energy range and suggests that a  
 618 break exists between the two energy ranges. Our joint spectral fit to the first of these three intervals  
 619 ( $t_0 \sim 300$  sec post trigger) shows that the broadband SED can be well described by a single electron

620 synchrotron spectrum with a cooling break between the X-ray and gamma-ray regimes, matching the  
 621 conclusions of Kouveliotou et al. (2013) at much later times.

622 The non-detection of IC emission is also notable in GRB 100728A and GRB 110213A, both of  
 623 which were detected by the LAT and which showed energetic X-ray flares and a significant X-ray  
 624 plateau lasting roughly  $\sim 2000$  sec, respectively. These light curve features have been proposed to  
 625 be the result of late-time energy injection due to continued activity of the central engine (Burrows  
 626 et al. 2005b; Fan & Wei 2005; Zhang et al. 2006; Panaitescu 2008) and SSC emission at GeV energies  
 627 could be expected in such a scenario. For both bursts, our analysis finds that the contemporaneous  
 628 XRT and LAT observations are consistent with a single spectral component. In the case of GRB  
 629 100728A we find weak evidence of a break in the broadband spectrum, consistent with a cooling  
 630 break in an electron synchrotron spectrum. **These results point to synchrotron-dominated  
 631 emission during the flare and plateau afterglow components, and the non-detection of  
 632 IC emission again suggests a shocked external medium with a strong magnetic field,  
 633 an extremely high  $\gamma_c$  value so as to have avoided the production of a dominant SSC  
 634 component at GeV energies, or a blast wave in the Klein-Nishina dominated regime so  
 635 as to suppress electron-photon scattering.**

## 636 7. CONCLUSIONS

637 We have used joint observations by the *Swift* XRT and the *Fermi* LAT of GRB afterglows to  
 638 investigate the nature of long-lived, high-energy emission observed by *Fermi* LAT. By extrapolating  
 639 the XRT derived spectra of *Swift*-detected GRBs, we compared the expected flux in the 0.1 to 100  
 640 GeV energy range to the LAT upper limits for the periods in which the burst position was within  
 641 the LAT FoV. We found that only a small subset of bursts exhibit afterglow emission that could  
 642 exceed the LAT detection threshold when extrapolated to the 0.1 to 100 GeV energy range. Bursts  
 643 that do result in late-time LAT detections are almost exclusively drawn from afterglows that exhibit  
 644 emission brighter than  $F_{\text{XRT}} \gtrsim 10^{-10}$  erg cm $^{-2}$  s $^{-1}$  and harder than  $\Gamma_{\text{XRT}} \lesssim 2$ .

645 Joint broadband spectral fits of XRT and LAT data reveal that a majority of LAT non-detections  
 646 of relatively bright X-ray afterglows can be explained by an afterglow spectrum with a slightly softer  
 647 photon index when constrained by both the XRT and LAT data, compared to the photon index  
 648 derived by fits to the XRT data alone. The remaining LAT non-detections are consistent with a  
 649 cooling break in the predicted electron synchrotron spectrum between the XRT and LAT energy  
 650 ranges. Such a break is sufficient to suppress the high-energy emission below the LAT detection  
 651 threshold. On the other hand, the broadband spectra of LAT-detected bursts are best modeled by  
 652 spectral components that indicate that the cooling break in the synchrotron spectrum lies either  
 653 between or above the XRT and LAT energy ranges.

654 Since the value and time evolution of the cooling frequency in an electron synchrotron spectrum is  
 655 strongly dependent on the density profile of the circumstellar medium, we speculate that the primary  
 656 difference between bursts with afterglow detections by the LAT and the non-detected population may  
 657 be the type of circumstellar environment. Late-time LAT detections may be preferentially selecting  
 658 GRBs that occur in low-density wind-like circumburst environments for which the synchrotron cooling  
 659 break begins near the X-ray regime and does not evolve to lower energies, resulting in an afterglow  
 660 spectrum above the X-ray regime that remains spectrally hard for longer periods of time, enhancing  
 661 the detectability of the afterglow in the LAT energy range.



662 We find no evidence of high-energy emission significantly in excess of the flux expected from the  
663 spectrum predicted by the electron synchrotron model. In addition, joint spectral fits of contempo-  
664 raneous XRT and LAT observations of an episode of energetic X-ray flaring in GRB 100728A and a  
665 significant X-ray plateau in GRB 110213A find that the XRT and LAT data are consistent with a  
666 single spectral component. The lack of excess emission at high energies points to two possibilities: 1)  
667 a shocked external medium in which the energy density in the magnetic field is elevated or compa-  
668 rable to that of the relativistic electrons behind the shock, precluding the production of a dominant  
669 SSC component in the LAT energy range at late times, or 2) the peak of the SSC emission is beyond  
670 the 0.1 to 100 GeV energy range we considered.

671 The *Fermi* LAT Collaboration acknowledges generous ongoing support from a number of agencies and  
672 institutes that have supported both the development and the operation of the LAT as well as scientific  
673 data analysis. These include the National Aeronautics and Space Administration and the Department  
674 of Energy in the United States, the Commissariat à l’Energie Atomique and the Centre National de  
675 la Recherche Scientifique / Institut National de Physique Nucléaire et de Physique des Particules  
676 in France, the Agenzia Spaziale Italiana and the Istituto Nazionale di Fisica Nucleare in Italy, the  
677 Ministry of Education, Culture, Sports, Science and Technology (MEXT), High Energy Accelerator  
678 Research Organization (KEK) and Japan Aerospace Exploration Agency (JAXA) in Japan, and the  
679 K. A. Wallenberg Foundation, the Swedish Research Council and the Swedish National Space Board  
680 in Sweden.

681 Additional support for science analysis during the operations phase is gratefully acknowledged from  
682 the Istituto Nazionale di Astrofisica in Italy and the Centre National d’Études Spatiales in France.  
683 This work performed in part under DOE Contract DE-AC02-76SF00515.

## REFERENCES

- 684 Abdo, A. A., Ackermann, M., Arimoto, M., et al. 730  
685 2009a, *Science*, 323, 1688,  
686 doi: [10.1126/science.1169101](https://doi.org/10.1126/science.1169101)
- 687 Abdo, A. A., Ackermann, M., Asano, K., et al. 731  
688 2009b, *ApJ*, 707, 580,  
689 doi: [10.1088/0004-637X/707/1/580](https://doi.org/10.1088/0004-637X/707/1/580)
- 690 Abdo, A. A., Ackermann, M., Ajello, M., et al. 732  
691 2011, *ApJL*, 734, L27,  
692 doi: [10.1088/2041-8205/734/2/L27](https://doi.org/10.1088/2041-8205/734/2/L27)
- 693 Acero, F., Ackermann, M., Ajello, M., et al. 2015, 733  
694 *ApJS*, 218, 23,  
695 doi: [10.1088/0067-0049/218/2/23](https://doi.org/10.1088/0067-0049/218/2/23)
- 696 Ackermann, M., Ajello, M., Baldini, L., et al. 734  
697 2010, *ApJL*, 717, L127,  
698 doi: [10.1088/2041-8205/717/2/L127](https://doi.org/10.1088/2041-8205/717/2/L127)
- 699 Ackermann, M., Ajello, M., Albert, A., et al. 735  
700 2012a, *ApJS*, 203, 4,  
701 doi: [10.1088/0067-0049/203/1/4](https://doi.org/10.1088/0067-0049/203/1/4)
- 702 Ackermann, M., Ajello, M., Baldini, L., et al. 736  
703 2012b, *ApJ*, 754, 121,  
704 doi: [10.1088/0004-637X/754/2/121](https://doi.org/10.1088/0004-637X/754/2/121)
- 705 Ackermann, M., Ajello, M., Asano, K., et al. 737  
706 2013a, *ApJ*, 763, 71,  
707 doi: [10.1088/0004-637X/763/2/71](https://doi.org/10.1088/0004-637X/763/2/71)
- 708 —. 2013b, *ApJS*, 209, 11,  
709 doi: [10.1088/0067-0049/209/1/11](https://doi.org/10.1088/0067-0049/209/1/11)
- 710 —. 2014, *Science*, 343, 42,  
711 doi: [10.1126/science.1242353](https://doi.org/10.1126/science.1242353)
- 712 Ackermann, M., Ajello, M., Anderson, B., et al. 738  
713 2016, *ApJ*, 822, 68,  
714 doi: [10.3847/0004-637X/822/2/68](https://doi.org/10.3847/0004-637X/822/2/68)
- 715 Arnaud, K. A. 1996, in *Astronomical Society of*  
716 *the Pacific Conference Series*, Vol. 101,  
717 *Astronomical Data Analysis Software and*  
718 *Systems V*, ed. G. H. Jacoby & J. Barnes, 17
- 719 Atwood, W. B., Abdo, A. A., Ackermann, M.,  
720 et al. 2009, *ApJ*, 697, 1071,  
721 doi: [10.1088/0004-637X/697/2/1071](https://doi.org/10.1088/0004-637X/697/2/1071)
- 722 Barthelmy, S. D., Barbier, L. M., Cummings,  
723 J. R., et al. 2005, *SSRv*, 120, 143,  
724 doi: [10.1007/s11214-005-5096-3](https://doi.org/10.1007/s11214-005-5096-3)
- 725 Beloborodov, A. M., Hascoët, R., & Vurm, I.  
726 2014a, *ApJ*, 788, 36,  
727 doi: [10.1088/0004-637X/788/1/36](https://doi.org/10.1088/0004-637X/788/1/36)
- 728 —. 2014b, *ApJ*, 788, 36,  
729 doi: [10.1088/0004-637X/788/1/36](https://doi.org/10.1088/0004-637X/788/1/36)
- 730 Beniamini, P., Guetta, D., Nakar, E., & Piran, T.  
731 2011, *MNRAS*, 416, 3089,  
732 doi: [10.1111/j.1365-2966.2011.19259.x](https://doi.org/10.1111/j.1365-2966.2011.19259.x)
- 733 Burrows, D. N., Hill, J. E., Nousek, J. A., et al.  
734 2005a, *SSRv*, 120, 165,  
735 doi: [10.1007/s11214-005-5097-2](https://doi.org/10.1007/s11214-005-5097-2)
- 736 Burrows, D. N., Romano, P., Falcone, A., et al.  
737 2005b, *Science*, 309, 1833,  
738 doi: [10.1126/science.1116168](https://doi.org/10.1126/science.1116168)
- 739 Cenko, S. B., Frail, D. A., Harrison, F. A., et al.  
740 2011, *ApJ*, 732, 29,  
741 doi: [10.1088/0004-637X/732/1/29](https://doi.org/10.1088/0004-637X/732/1/29)
- 742 Chevalier, R. A., & Li, Z.-Y. 2000, *ApJ*, 536, 195,  
743 doi: [10.1086/308914](https://doi.org/10.1086/308914)
- 744 De Pasquale, M., Schady, P., Kuin, N. P. M.,  
745 et al. 2010, *ApJL*, 709, L146,  
746 doi: [10.1088/2041-8205/709/2/L146](https://doi.org/10.1088/2041-8205/709/2/L146)
- 747 Dermer, C. D., Chiang, J., & Mitman, K. E. 2000,  
748 *ApJ*, 537, 785, doi: [10.1086/309061](https://doi.org/10.1086/309061)
- 749 Evans, P. A., Beardmore, A. P., Page, K. L., et al.  
750 2007, *A&A*, 469, 379,  
751 doi: [10.1051/0004-6361:20077530](https://doi.org/10.1051/0004-6361:20077530)
- 752 —. 2009, *MNRAS*, 397, 1177,  
753 doi: [10.1111/j.1365-2966.2009.14913.x](https://doi.org/10.1111/j.1365-2966.2009.14913.x)
- 754 Fan, Y., & Piran, T. 2006, *MNRAS*, 370, L24,  
755 doi: [10.1111/j.1745-3933.2006.00181.x](https://doi.org/10.1111/j.1745-3933.2006.00181.x)
- 756 Fan, Y. Z., & Wei, D. M. 2005, *MNRAS*, 364,  
757 L42, doi: [10.1111/j.1745-3933.2005.00102.x](https://doi.org/10.1111/j.1745-3933.2005.00102.x)
- 758 Ghisellini, G., Ghirlanda, G., Nava, L., & Celotti,  
759 A. 2010, *MNRAS*, 403, 926,  
760 doi: [10.1111/j.1365-2966.2009.16171.x](https://doi.org/10.1111/j.1365-2966.2009.16171.x)
- 761 Granot, J., & Sari, R. 2002, *ApJ*, 568, 820,  
762 doi: [10.1086/338966](https://doi.org/10.1086/338966)
- 763 He, H.-N., Zhang, B.-B., Wang, X.-Y., Li, Z., &  
764 Mészáros, P. 2012, *ApJ*, 753, 178,  
765 doi: [10.1088/0004-637X/753/2/178](https://doi.org/10.1088/0004-637X/753/2/178)
- 766 Kouveliotou, C., Granot, J., Racusin, J. L., et al.  
767 2013, *ApJL*, 779, L1,  
768 doi: [10.1088/2041-8205/779/1/L1](https://doi.org/10.1088/2041-8205/779/1/L1)
- 769 Kumar, P., & Barniol Duran, R. 2009, *MNRAS*,  
770 400, L75, doi: [10.1111/j.1745-3933.2009.00766.x](https://doi.org/10.1111/j.1745-3933.2009.00766.x)
- 771 Mattox, J. R., Bertsch, D. L., Chiang, J., et al.  
772 1996, *ApJ*, 461, 396, doi: [10.1086/177068](https://doi.org/10.1086/177068)
- 773 Maxham, A., Zhang, B.-B., & Zhang, B. 2011,  
774 *MNRAS*, 415, 77,  
775 doi: [10.1111/j.1365-2966.2011.18648.x](https://doi.org/10.1111/j.1365-2966.2011.18648.x)
- 776 Neyman, J., & Pearson, E. S. 1928, *Biometrika*,  
777 20, 175, doi: [10.1007/s11214-005-5097-2](https://doi.org/10.1007/s11214-005-5097-2)

- 778 Panaitescu, A. 2008, MNRAS, 383, 1143,  
779 doi: [10.1111/j.1365-2966.2007.12607.x](https://doi.org/10.1111/j.1365-2966.2007.12607.x)
- 780 Racusin, J. L., Oates, S. R., de Pasquale, M., &  
781 Kocevski, D. 2016, ApJ, 826, 45,  
782 doi: [10.3847/0004-637X/826/1/45](https://doi.org/10.3847/0004-637X/826/1/45)
- 783 Racusin, J. L., Liang, E. W., Burrows, D. N.,  
784 et al. 2009, ApJ, 698, 43,  
785 doi: [10.1088/0004-637X/698/1/43](https://doi.org/10.1088/0004-637X/698/1/43)
- 786 Racusin, J. L., Oates, S. R., Schady, P., et al.  
787 2011, ApJ, 738, 138,  
788 doi: [10.1088/0004-637X/738/2/138](https://doi.org/10.1088/0004-637X/738/2/138)
- 789 Razzaque, S., Dermer, C. D., & Finke, J. D. 2010,  
790 The Open Astronomy Journal, 3, 150,  
791 doi: [10.2174/1874381101003010150](https://doi.org/10.2174/1874381101003010150)
- 792 Roming, P. W. A., Kennedy, T. E., Mason, K. O.,  
793 et al. 2005, SSRv, 120, 95,  
794 doi: [10.1007/s11214-005-5095-4](https://doi.org/10.1007/s11214-005-5095-4)
- 795 Sari, R., & Esin, A. A. 2001, ApJ, 548, 787,  
796 doi: [10.1086/319003](https://doi.org/10.1086/319003)
- 797 Schulze, S., Klose, S., Björnsson, G., et al. 2011,  
798 A&A, 526, A23,  
799 doi: [10.1051/0004-6361/201015581](https://doi.org/10.1051/0004-6361/201015581)
- 800 Tam, P.-H. T., Tang, Q.-W., Hou, S.-J., Liu,  
801 R.-Y., & Wang, X.-Y. 2013, ApJL, 771, L13,  
802 doi: [10.1088/2041-8205/771/1/L13](https://doi.org/10.1088/2041-8205/771/1/L13)
- 803 Vianello, G., Omodei, N., & Fermi/LAT  
804 collaboration. 2015, ArXiv e-prints.  
805 <https://arxiv.org/abs/1502.03122>
- 806 Wang, X.-Y., Liu, R.-Y., & Lemoine, M. 2013,  
807 ApJL, 771, L33,  
808 doi: [10.1088/2041-8205/771/2/L33](https://doi.org/10.1088/2041-8205/771/2/L33)
- 809 Wilks, S. S. 1938, Ann. Math. Statist., 9, 60,  
810 doi: [10.1214/aoms/1177732360](https://doi.org/10.1214/aoms/1177732360)
- 811 Yassine, M., Piron, F., Mochkovitch, R., &  
812 Daigne, F. 2017, A&A, 606, A93,  
813 doi: [10.1051/0004-6361/201630353](https://doi.org/10.1051/0004-6361/201630353)
- 814 Zhang, B., Fan, Y. Z., Dyks, J., et al. 2006, ApJ,  
815 642, 354, doi: [10.1086/500723](https://doi.org/10.1086/500723)
- 816 Zhang, B., & Mészáros, P. 2001, ApJ, 559, 110,  
817 doi: [10.1086/322400](https://doi.org/10.1086/322400)
- 818 Zhang, B.-B., Zhang, B., Liang, E.-W., et al.  
819 2011, ApJ, 730, 141,  
820 doi: [10.1088/0004-637X/730/2/141](https://doi.org/10.1088/0004-637X/730/2/141)